Block-Copolymer-derived plasmonic templates and its applications

Trinity College Dublin
Coláiste na Tríonóide, Baile Átha Cliath
The University of Dublin

A Master thesis submitted to the School of Chemistry by

Gökalp Engin Akinoglu

Under the supervision

Prof. Mokarian-Tabari

January 25, 2021

I declare that this report details entirely my own work. Due acknowledgements and references are given to the work of others where appropriate.


…… Gökalp Engin Akinoglu

Die Esel sind ausgezogen um Hörner zu suchen

und sind ohne Ohren heimgekehrt

Publication list

Akinoglu, G.E., Akinoglu, E. M., Kempa, K and Giersig, M., Plasmon resonances in coupled Babinet complementary arrays in the mid-infrared range. Optics Express, 2019, 27(16), p. 22939-22950.

Akinoglu, G. E., Mir, S. H., Gatensby, R., Rydzek, G., Mokarian-Tabari, P., Block Copolymer Derived Vertically Coupled Plasmonic Arrays for Surface-Enhanced Raman Spectroscopy. ACS Applied Materials & Interfaces 2020, *12* (20), p. 23410-23416.

Akinoglu E. M., Luo L., Tod T., Gou L., **Akinoglu G. E.**, Wang X., Shui L., Zhou G., Naughton M. J., Kempa K. and Giersig M., Extraordinary optical transmission in nano-bridged plasmonic arrays mimicking a stable weakly connected percolation threshold. Optics Express (Just accepted)

Abstract

Plasmonic metasurfaces have important applications in life science, optics, and catalysis. However, their industrial usage is limited by high throughput nanofabrication. A promising solution is the transfer of a pattern into a substrate using block copolymers, nanostructured stamps or molds to create binary, three dimensional templates, which can then be decorated with plasmon active metals. Here, the optical properties of quasi-Babinet complementary arrays in the non-retarded regime is investigated by finite-difference time-domain simulations. The structures consist of a nanopillar support, which is covered with metal disks on top of the pillars and a quasi-Babinet complementary perforated film consisting of a hexagonal arranged hole array at the base of the pillars. Strong vertical plasmonic coupling occurs for small separation distances of the plasmonic slabs. The thesis presents a comprehensive study of the near and far-field properties of such vertically coupled plasmonic arrays varying their geometric dimension and the employed metals with their intrinsic plasmonic material properties. In particular, gold, silver, copper, aluminum, nickel, and palladium are considered. Furthermore, the effect of the refractive index of the nanopillar support is investigated. The plasmonic slabs show tunable extraordinary transmission and large electric near-field enhancements, which is strongly dependent on the employed material and geometry. Further, it is shown that the templates are suitable for plasmonic hetero-structures commonly used in plasmon-enhanced photocatalysis.

Finally, the thesis reports on a block copolymer derived vertically coupled plasmonic template for surface enhanced Raman spectroscopy. Nanopillar templates were fabricated by the incorporation of an iron salt precursor into a self-assembled block copolymer thin film and subsequent reactive ion etching. Subsequently, the nanopillars were coated with gold to create quasi

Babinet complementary plasmonic templates. An increase of surface enhanced Raman scattering efficiency for smaller pillar heights and stronger coupling between the dot array and perforated gold film with average enhancement factors as high as 10^7 is observed. In addition, the block copolymer derived templates show an excellent relative standard deviation of the Raman intensity up to 8%.

Contentsa

1. Introduction

Plasmons are the collective oscillations of free electrons that can be excited in conductive nanomaterials at their optical resonance. Due to their capability to modulate light and enhance light-matter interaction they have found an increasing interest in the last decades. Plasmonic nanomaterials can be used for color printing, where individual color pixels can be fabricated beyond the diffraction limit [1-4], for optical filters [5, 6], photothermal cancer therapies[7] or for colorimetric sensors[8]. On the other hand, plasmons confine the light at the nanoparticle interfaces. The increased electric near-fields can be used for the enhancement of physical or chemical processes and reactions. As an example plasmons can facilitate enhanced catalysis[9] or can be used to enhance molecular sensing such as for surface enhanced Raman spectroscopy [10-12], surface enhanced infrared spectroscopy[13] or surface enhanced fluorescence spectroscopy [14, 15]. The plasmon resonance can be adjusted by size, shape and arrangement of the nanoparticles for their particular purpose.

Many different methods exist of fabricating plasmonic nanomaterials[6, 12, 16, 17]. However, many plasmon based applications have yet to be used outside of academic research, because cost-effective, scalable and reproducible methods of producing plasmonic templates are currently not available for a wide range of industrial problems [18]. One of the promising methods to overcome this issue is block copolymer lithography[19]. Block copolymers consist of two or more blocks of polymers. Depending on the volume fraction of the blocks and their chemical nature they can self-assemble into periodic arrays with geometric dimensions between 3 - 100 nm[20], although larger dimensions have been reported[21]. Metallic precursors can be selectively incorporated into one of the polymer blocks [22-24]. This can be used to fabricate periodically arranged dot arrays of a perforated thin film consisting of periodically arranged holes (fig. 1(A) and (C)).

One can also incorporate etch resistto form a hard mask or use one of the blocks of the block copolymer mask as a soft mask to transfer the pattern into the substrate[20]. Subsequently, the etched template can be deposited with plasmon active material to create three-dimensional plasmonic templates such as coated nano pillar and cavity ararys (fig. 1(B) and (D)). They consist of a dot array and a Babinet complementary perforated thin film, that can form vertically coupled plasmonic arrays[6]. The coated pillar and cavity array look from top down identical. However, the dot array and perforated film are at different planes.

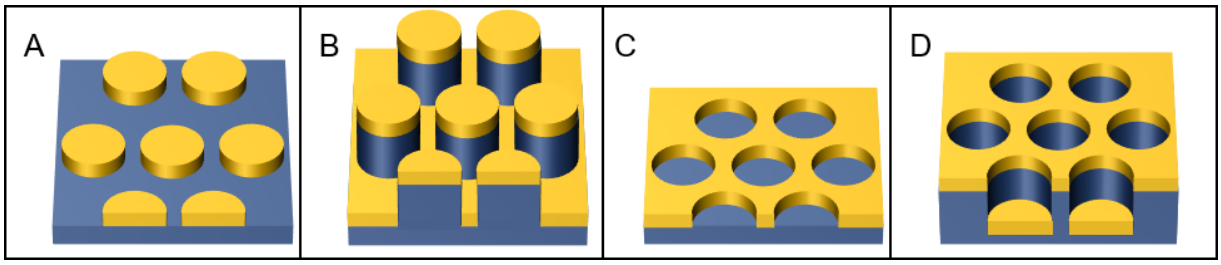

Figure 1. Possible hexagonal configurations of block copolymer derived plasmonic templates. (A) Dot array. (B) Coated pillar array. (C) Perforated thin film consisting of arranged holes. (D) Coated cavity array.

This first chapter will give an introduction on the fundamentals of plasmon excitations and the modelling of the plasmon resonances. An emphasis will be put on Babinet complementary plasmonic arrays in the infrared region. The next chapter will give a short introduction on experimental methods with a focus on block copolymers. In the fourth chapter of the thesis results on the optical far- and near-field properties of vertically coupled plasmonic arrays in the visible regime are presented and discussed. In this regime the plasmon dispersion deviates from the light line and is governed by Mie resonances which are highly material dependent. Subsequently, it is shown that block copolymer derived vertically coupled plasmonic arrays plasmonic arrays can be used as a surface enhanced Raman template. However, the fundamental principles are universal and the plasmonic templates are suitable for other electric near-field based methods.

2. Experimental fundamentals and methods

2.1 Block copolymer lithography and its applications

Block copolymer lithography is a versatile method to nanotexture surfaces on a large scale for different applications. For example, block copolymer can be used to directly incorporate precursors into one of the blocks that are subsequently plasmonic active. These precursors are generally salts of noble metals such as gold[22], silver[23] or platinum[24]. They can be reduced by plasma treatment or a reducing agent. The advantage of the preparation is that it does not require a vacuum based deposition system such as e-beam evaporation or magnetron sputtering. Although, noble metal salts are considerably more expansive than the corresponding bulk metal. However, the reduction of noble metal salts can be also easily performed in solution [25] and hence it has to be justified to use a lithographic approach. The plasmonic response of such nanoparticle arrays can be tailored by their geometric parameters of the system [22-24] or the effective refractive index of the environment[26] (more in the chapter surface plasmons). The distinct plasmonic extinction can manifest as structural colour. In combination with a stimuli responsive polymers plasmonic templates [27, 28] can be used as colorimetric sensors if the stimuli alters the configuration of the plasmonic template or the refractive index of their surroundings. As an example polydimethylsiloxane (PDMS) is a stretchable polymer and it has been shown that a block derived plasmonic template on PDMS can be used as an colorimetric strain sensor[29]. The concept can be expanded to other stimuli responsive materials to fabricate humidity, temperature, pH or pressure sensors[27, 28]. A concept of the principle mechanism is illustrated in figure 2.1 (A).

Aluminium has been recently discovered as a promising plasmonic material[30]. It is cheap, abundantly available and is plasmon active for a wide spectral range including the ultraviolet[30].

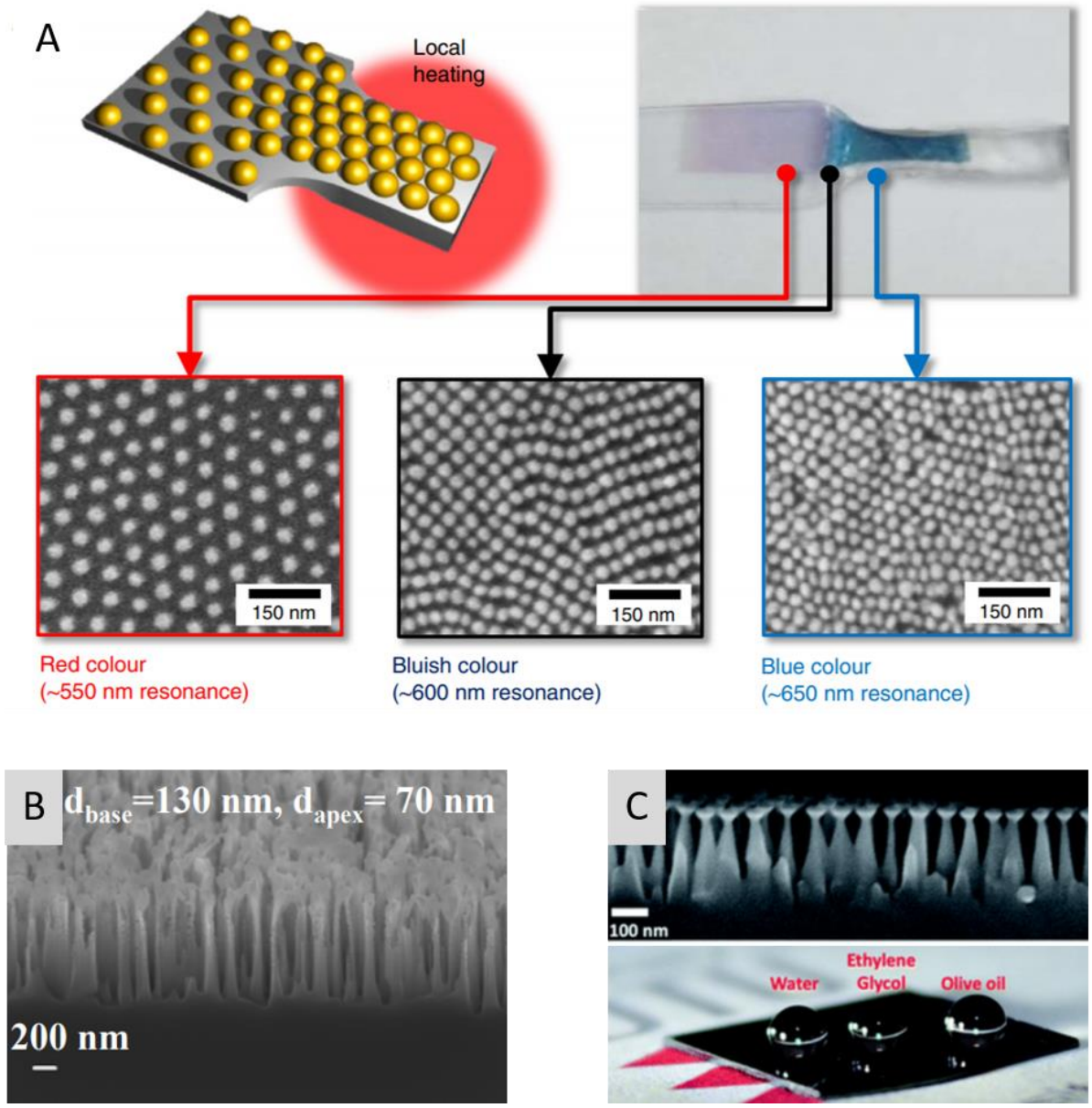

Figure 2.1 Different block copolymer lithography derived templates and its applications (A) Plasmonic nanoparticles template on a stimuli responsive polymer. The change of the inter particle distance results in a change of colour. Adapted from Ref. [29]. (B) Nanopillar template that form an effective medium with a graded refractive index. The template featured reduced reflection over a broad spectrum. Adopted from Ref. [21]. (C) Functionalized nanohoodoo template with superamphiphobic properties. Adopted from Ref. [31]

Due to its native oxide layer aluminium nanoparticles feature only small electric near-field enhancements. Yet, aluminium is still attractive for colorimetric sensors or other far-field based applications[32]. However, the effective wet chemical preparation of aluminium nanoparticles is

still an active field of research[33] and the fabrication by e-beam lithography suffers again from the lack of scalability. However, aluminium precursor can be easily infiltrated into block co-polymer templates[34]. Generally, oxygen plasma or UV ozone treatment is used to subsequently remove the polymer pattern. However, this would result in oxidation of the aluminium precursor. Instead one could use hydrogen plasma that is reducing [35] and subsequently cover the aluminium array with a protection layer for any subsequent oxidation. The layer could also consist of a stimuli responsive polymer for a colorimetric sensor.

Furthermore, block copolymer lithography can be used to transfer a pattern into a substrate in order to nanostructure the substrate surface. For example block copolymer derived nanopillar templates have been used to create anti-reflective layers on curved surfaces[36, 37]. The surface texturing resembles that of a Moth eye and suppresses surface reflection over a broad spectrum[21],which is an important criteria in optical elements such as implemented in continuum lasers for example [38]. The moth eye structures are an effective medium that provide a graded refractive index (see fig. 2.1(B))[39]. An important factor for optics is that the structure does not only feature minimal reflection but also high transmission without losses caused by scattering. Alternatively, it has been shown that block copolymer derived nanohoodoos that were subsequently functionalized can have superhydrophobic, superhydrophilic, or superamphiphobic properties[31] (see fig. 2.1(C)).

2.2 Block copolymers

Block copolymers consist of two or more strands (blocks) of different polymers that are covalently attached to each other. Depending on the length and the chemical nature of the blocks, block copolymers can undergo reversible and spontaneous self-assembly into distinct morphologies. The thermodynamics of self-assembly can be expressed by the change in the Gibbs free energy. The Gibbs free energy is a thermodynamic potential that can be used to calculate the maximum non-volume work, which is performed at constant temperature *T* and pressure:

$$\Delta \mathrm{G} = \Delta \mathrm{H} - \mathrm{T}\Delta \mathrm{S} \tag{2.1}$$

where $\Delta \mathrm{H}$ is the change in enthalpy and $\Delta \mathrm{S}$ is the change in entropy. Self-assembly is spontaneous if the difference in Gibbs free energy $\Delta \mathrm{G}_{SA}$ is negative.

$$\Delta \mathrm{G}_{SA} = \mathrm{G}_{mix} - G_{phase\ saperated} = \Delta \mathrm{H}_{SA} - \mathrm{T}\Delta \mathrm{S}_{SA} < 0 \tag{2.2}$$

where T is the temperature and ΔH_{SA} and ΔS_{SA} is the change is enthalpy and entropy before and after self-assembly. The process is spontaneous if the Gibbs free energy is negative.

In the case of a blend of two homopolymers A and B, the degree of polymerization is defined as $N=N_A+N_B$ and the composition $1=f_A+f_B$. The process of self-assembly is then described by the Flory–Huggins equation:

$$\frac{\Delta \mathrm{G}}{\mathrm{k_b T}} = \frac{1}{\mathrm{N_A}} ln(\mathrm{f_a}) + \frac{1}{\mathrm{N_B}} ln(\mathrm{f_B}) + \mathrm{f_A}\,\mathrm{f_B}\chi \tag{2.3}$$

The first two terms correspond to the configurational entropy of the system. The third term relates to the molar enthalpy of mixing and describes the unfavorable interaction of A-B monomers. χ is the exchange energy per molecule and is known as the Flory–Huggins interaction parameter. It is a function of both the chemical nature of the polymer blocks and temperature. In general, it has the form:

$$\chi = \frac{a}{T} + b \tag{2.4}$$

where *a* and *b* are variables for a specific composition of a particular block copolymer and can be experimentally obtained [40]. It can be theoretically derived that the morphology of block copolymer can be direclty related to the ratio bewteenl χN versus f [41]. The phase diagram can be seen in figure 2.2. Different ratios result in cubic, hexagonal, gyroid or lamellar morphologies. However, χN value has to be above 10.5 for ordered morphologies to occur[41].

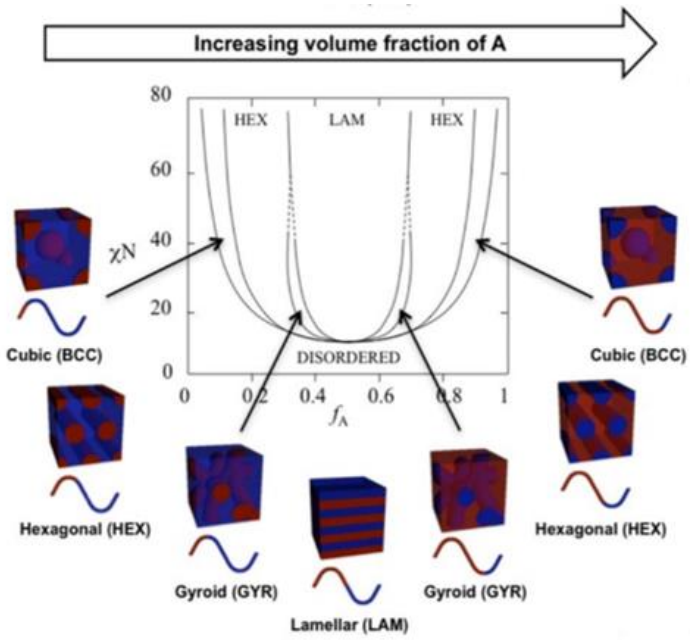

Figure 2.2 Theoretical phase diagram and evolution of corresponding morphologies in BCP. Adopted from Ref. [37].

2.3 Solvent vapor annealing

Microphase separation of block copolymers require long annealing times and temperatures above the glass transition temperature. In the case of large molecular weight polymers and or-

dered equilibrium states a simple thermal treatment may not be sufficient[42]. This can be overcome in solvent vapour annealing where the prepared block copolymer thin films are exposed to solvent vapour of one or more solvents well below the bulk glass transition temperature. The solvent vapour creates a swollen state and mobilises the polymer chains leading to a phase separation. In addition, the solvent exposure lowers the glass transition temperature so that thermal annealing can occur naturally[42]. In a standard solvent vapour annealing procedure, a reservoir of solvent is placed in a jar next to block copolymer patterned substrates (fig. 2.3(A)). The jar is placed in an oven, the solvent evaporates and facilitates microphase separation of the block copolymer. In figure 2.3(B) we can see a solvent vapour annealed Ps-*b*-PEO (M_{PS}=42 kg mol^{-1} and M_{PEO}=11.5 kg mol) block copolymer film in hexagonal morphology. However, the final state of the block copolymer is not always stable, meaning it is not trapped in one minima of

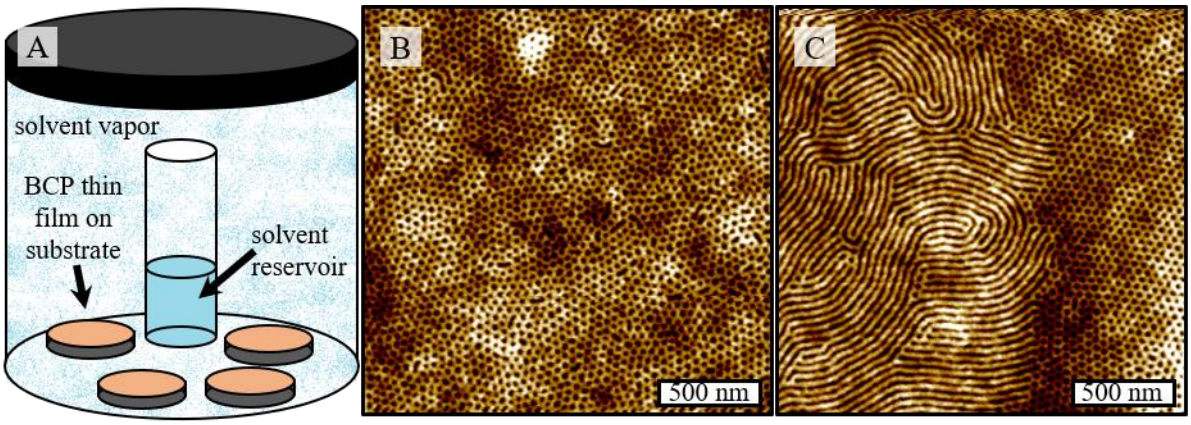

Figure 2.3 (A) Solvent vapor annealing in a jar. (B) AFM image of a complete hexagonal pattern and (C) mixed lamellar and hexagonal pattern of a PS-b-PEO film.

the potential energy landscape and can flip between states[43]. This is shown in figure 2.3(C) where one can see a mixed lamellar/hexagonal morphology of the same PS-*b*-PEO film.

2.4 Inclusion of inorganics

Block copolymer lithography has been used to transfer an inorganic template onto a substrate[20]. Generally, the block copolymer film is swelled to activate one of the blocks for infiltration[20, 44]. A precursor is than spin coated on the block copolymer film or the block copolymer system is bathed in a solution with a precursor in order to infiltrate the block copolymer system[20]. However, there are also other techniques such as solvent vapor inclusion to infiltrate inorganics in the block copolymer system[45]. Subsequently, the organics can be removed via UV/ozone or plasma treatment.[46] In figure 2.3(A) an iron oxide mask prepared with the previously shown PS-*b*-PEO system is shown. The morphology of the final mask can be altered by the block copolymer system or the infiltration of the precursor. Asan example, in figure 2.3(A) a porous nickel oxide mask was fabricated. A high molecular weight PS-*b*-P2VP (M_{PS}= 440 kg mol^{-1} and M_{P2VP}=353kg mol) block copolymer template was over-saturated with nickel(II) nitrate and subsequently underwent UV/ozone treatment.

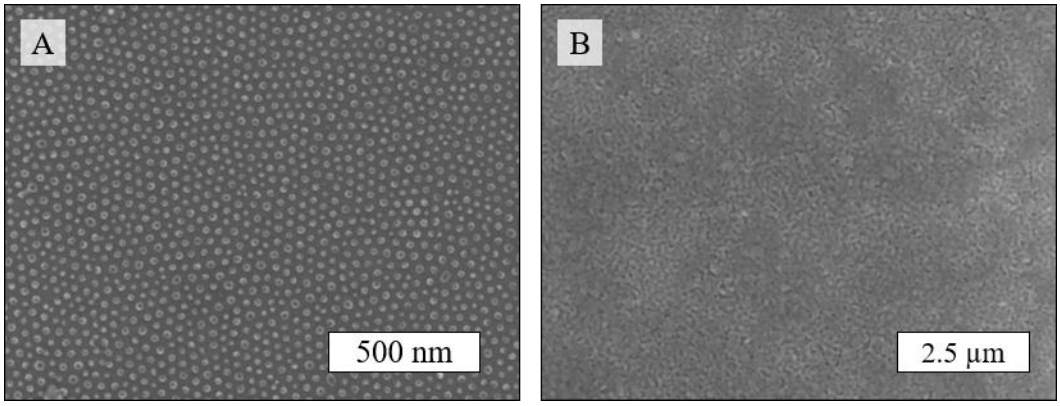

Figure 2.3 Block copolymer derived hard mask templates. (A) Iron oxide dot array prepared with PS-*b*-PEO. Porous nickel oxide template prepared with PS-*b*-P2VP.

2.5 Reactive ion etching

Common plasma etching of silicon and silicon oxides is performed in a reactive ion etcher (RIE) where the silicon is placed on a rf electrode [47]. The strong electric fields above the electrode result in a strong physical bombardment of the target sample with charged species. (I) Plasma generated neutral radicals chemically remove silicon, (II) a chemically inert passivation layer is deposited, so that chemical etching of silicon is hindered and (III) physical sputtering removes the passivated layer at the bottom of a trench, but not along the side. The exposed area is then unprotected for chemical removal. The etch/deposition cycles are repeated many times, resulting in a large number of small isotropic etch steps. An inert etched template can be used to specify the areas protected by the etching process. In addition, a process can be employed were all three steps occur simultaneously[48].

Reactive ion etching of silicon was performed in a OIPT Plasmalab System100 ICP180 etcher (Oxford instruments). The chamber atmosphere consisted of CHF_3, SF_6 and O_2 with a 9:1:1 gas ratio and a chamber pressure of 15 mTor. The ICP power was 1200W and the RF RIE power bias power was 35W. SF_6 is commonly used as process gas for the etching of silicon containing materials. In a plasma SF_6 undergoes a series of reactions resulting in the formation of fluorine radicals[49]:

$$\begin{aligned} S\,F_x + e &\rightarrow SF_{x-1}^- + F \\ &\rightarrow SF_{x-1} + F^- \\ &\rightarrow SF_{x-1} + F + e \qquad (x = 4 - 6) \end{aligned} \tag{2.5}$$

The free fluorine atoms can than react with silicon through the formation of SiF_4 [49]. SF_4 and other byproducts are very toxic and corrosive. CHF_3 on the other hand can react to CHF_2 in the

plasma, which can form a *Teflon* like passivation layer on the surface of the substrate. Ions produced as byproducts in the plasma can physically etch away the passivation layer at the bottom of the trenches. Finally, the etch depth can be adjusted by the etching time. An example of an etched template can be seen in figure 2.4(B).

Ideally, the etch mask is inert to neutral radicals and should only be degraded by physical etching of charged radicals. Etch resistance of the etch mask will depend on the used etch mask that can be altered by the used block copolymer and precursor used to infiltrate in the block copolymer systems.[20]

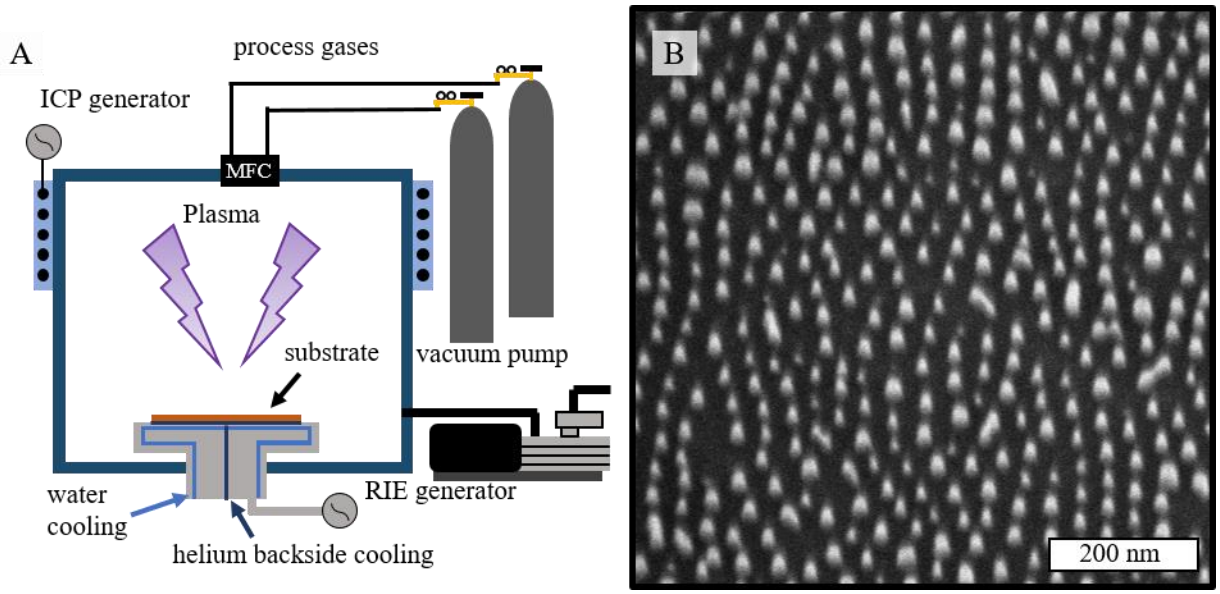

Figure 2.4. (A) Setup of the OIPT Plasmalab System100 ICP180 etcher. (B) Angled SEM view of etched silicon substrate. The white dots on top of the nanopillars are residues of the hard mask.

3. Fundamentals in plasmons: Theory and modelling

3.1 Surface plasmons

Plasmonics is the study of conductors and their interaction with an electromagnetic radiation[50]. It considers the presence of a plasma state of free electrons which collectively oscillate in a background of positively charged ions. The corresponding oscillation resonance is given by the plasma frequency ω_p:

$$\omega_p = \sqrt{\frac{4\pi n e^2}{m_e}} \tag{3.1}$$

where *n* is the electron density, *e* the elementary charge and m_e the electron mass. The plasma frequency is the most fundamental property of a plasma. Electromagnetic waves with frequency lower than ω_p cannot propagate through the plasma. Their response to an electrical field are described by the dielectric function $\epsilon(\omega)$ which is given in a first approximation by the Drude-Sommerfeld model[51]:

$$\epsilon(\omega) = 1 - \frac{\omega_p^2}{\omega^2} \tag{3.2}$$

inserting the dispersion relation for transverse waves propagating through uniform medium (solved by Telegrapher's equations)[26]:

$$k = \frac{\omega}{c}\epsilon(\omega) \tag{3.3}$$

yields

$$k(\epsilon) = \frac{\sqrt{\omega^2 - \omega_p^2}}{c} \tag{3.4}$$

where *c* is the speed and *k* the wave vector of the light. This is the dispersion relation of transverse volume plasmon polariton and is depicted as the red solid line in figure 3.1(A). For $\omega_p <$

ω the wave factor of the light becomes imaginary and only light with frequencies above the plasmon frequency have a wave vector with real values and can therefore propagate through a given medium. In addition to the transverse volume plasmon, a longitudinal bulk plasmon exist. They are an allowed solution of Maxwell's equations when the dielectric function of the plasma vanishes[50], but cannot be excited by transverse light (red dotted line in figure 3.1(A)).

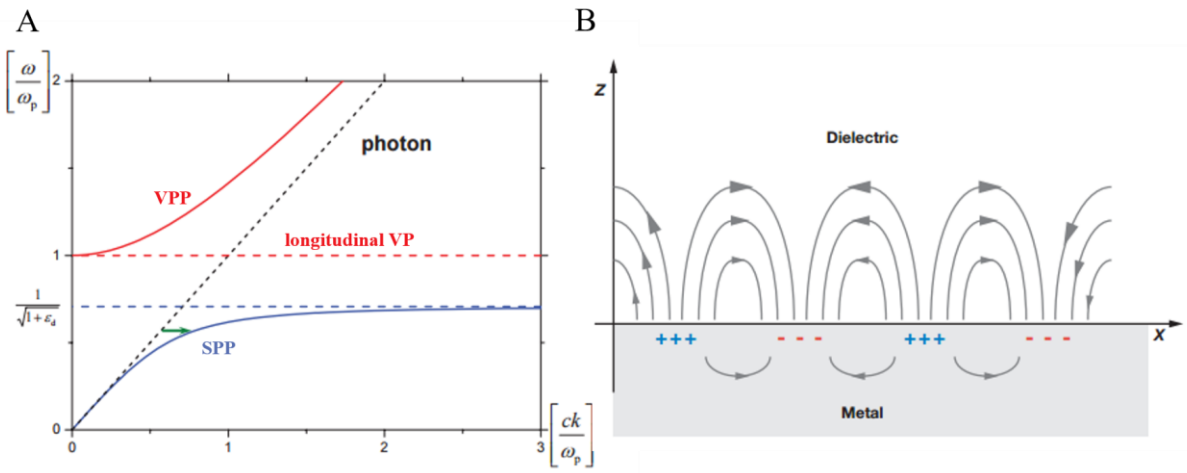

Figure 3.1 (A) Dispersion of volume plasmons (VP), surface plasmon polaritons (SSP) and photons. The green arrow illustrates the momentum missmtach between the light line ans SPP. Adopted and modified from [52]. (B) Visualation of a surface plasmon and its properties. Adopted from [53].

A different type of plasmon are surface plasmon polaritons (SPP), that constitute electromagnetic surface waves propagating along a conductor's surface with a broad spectrum of eigenfrequencies and modes (fig. 3.1(B))[50]. Their dispersion relation can be derived by Maxwell's equations at an interface with two different dielectric materials considering the continuity of the electromagnetic fields[54]:

$$k_x = \frac{\omega}{c}\sqrt{\frac{\epsilon_m \epsilon_d}{\epsilon_m + \epsilon_d}} \qquad (3.5)$$

As seen in figure 2(A) the SPP dispersion (blue solid branch) is always below the light line. Therefore, the excitation of SPP with light needs special light-plasmon coupler to compensate the momentum mismatch. This coupling can be achieved via a grating or an ATR prism[55]. In particular, if a photon hits a grating with a grating constant a at an angle θ, then its in-plane wave vector component can have values as:

$$k_x = \frac{\omega}{c}\sin(\theta) \pm \Delta k_x = k_{SP} \tag{3.6}$$

where $\Delta k_x = jG$ and where j is an integer and $G = \frac{2\pi}{a}$. The field amplitude of a SPP decreases exponentially normal to the surface and is described with the skin depth at which the field falls to 1/e. This is given by the imaginary part of the SPP wave vector in surface normal direction $\delta = |Im(k_z)|^{-1}$:

$$\delta_d = \frac{\lambda}{2\pi}\sqrt{\frac{e_m + e_d}{e_d^2}} \quad \text{in the dieelectric medium} \tag{3.7}$$

$$\delta_m = \frac{\lambda}{2\pi}\sqrt{\frac{e_m + e_d}{e_m^2}} \quad \text{in the metallic medium} \tag{3.8}$$

which yields for $\lambda = 600\,nm$ and silver-air interface $\delta_{d,air} = 390\,nm$ and $\delta_{m,Ag} = 24\,nm$ and for a gold interface $\delta_{d,air} = 280\,nm$ and $\delta_{m,Au} = 31\,nm$ respectively[55].

In geometries such as metallic particles or voids, localized surface plasmons (LSP) can be excited. When the size of the particle is much smaller than the wavelength of the light, the incident electric field is constant across the nanoparticle. Then the free electrons participate in a collective oscillation in phase with the light and confined by the boundaries of the object (see fig.

3.2(A)). The LSP resonance condition can be analytically solved for spheres by using Mie theory[56]

In general, the larger the particle, the smaller is the repulsion of electrons at opposite surfaces and the more red shifted is the resonance. The confinement of the oscillations also yields intense electric fields, which can be several magnitudes stronger than the incident field strength (fig. 3.2(B)) and can be exploited for molecular detection[53]. Summarizing, the size, shape and arrangement of plasmonic particles will determine the plasmonic response. For a particular application the plasmonic response can be adjusted by the choice of the block copolymer system used for lithography.

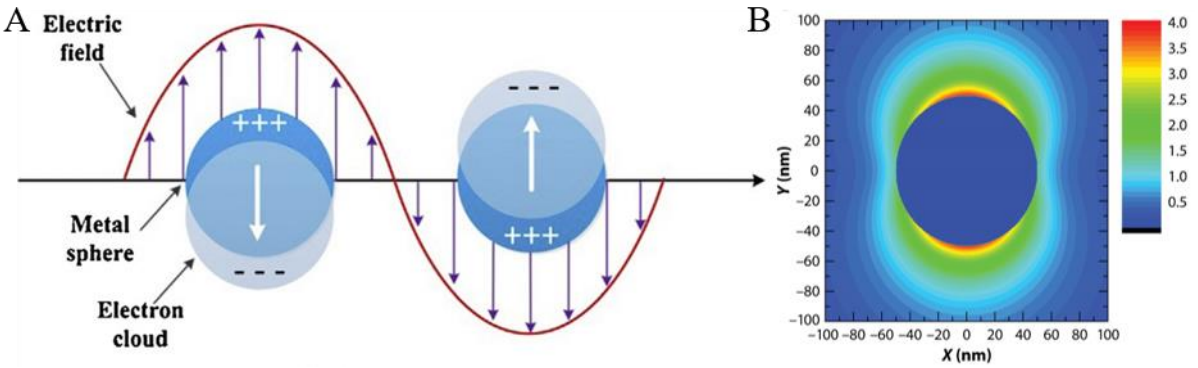

Figure 3.2 (A) Visualization of a surface plasmon of a metal nanosphere. Adopted from [53]. (B) Electric field amplitude $|E|$ for a 100 nm silver sphere, illuminated at a wavelength of 500 nm. Adopted from [57].

3.2 Babinet's principle

Babinet's principle relates the electromagnetic far-field respond of structures, made of infinitely thin films of a perfect conducting metal, to its complementary counterpart. In particular, it states that the transmittance T through complementary structures satisfies[58]:

$$T + T_C = 1 \tag{3.9}$$

Broad approximate validity of Babinet's principle extends to real metals, and films of finite thickness *d*, as long as $d/\lambda \ll 1$[50]. As an experimental limitation the minimal film thickness produced by vacuum deposition has to be generally above 15 nm to form a continuous film because the deposited metal can dewett on the surface[59]. However, it has been shown for many plasmonic systems that Babinet's principle holds true [6, 60-62].

3.3 Finite difference time domain simulation

The Finite Difference Time Domain (FDTD) method is a numerical approach to solve Maxwell equations and is commonly used to study the quantitative response of plasmonic structures exposed to electromagnetic radiation[63]. The FDTD algorithm solves the time evolution of the electric and magnetic fields, which are described by Faraday's induction law and Ampere's circuital law. They read in their differential form respectively:

$$\frac{d\vec{B}}{dt} = -\nabla \times \vec{E} - \overrightarrow{J_B} \tag{3.10}$$

$$\frac{d\vec{D}}{dt} = -\nabla \times \vec{H} - \vec{J} \tag{3.11}$$

where *E* and *H* are the macroscopic electric and magnetic fields, *D* and *B* are the electric displacement and magnetic induction fields, *J* is the electric-charge current density, and J_B is a fictitious magnetic-charge current density respectively (sometimes convenient in calculations, e.g. for magnetic-dipole sources).

In order to solve equation 3.10 and 3.11 numerically, the electric and magnetic field components have to be discretized in space and time into a grid. The grid suggested by Yee puts each field component at a different location of the Unit cell with half a pixel offset to the next field component (see fig. 3.3(A)). The time and space derivatives can then be formulated as center-difference approximations[64].

The simulations were performed with the freely available software package Meep[65]. The simulation cell is divided into a silicon and an air layer and the plasmonic array was placed on the interface (see fig. 3.3(B)). The source (Gaussian profile) is placed planar inside the silicon layer. Bloch-periodicity in all dimensions are used as a boundary condition. An artificial absorber layer hinders the transmission of light out of the cell in y direction, through which simulations are effectively only periodic in x-y direction[66]. For sufficiently large thickness the absorber layer becomes reflectionless, so that the flux planes for transmission and reflection collect the correct amount of light.

The flux planes monitor the power P(t) flowing through an area of interest and time. In case of a short pulse, the Fourier-transformed response yields a wavelength depended spectrum $P(\omega)$.The power $P(\omega)$ is normalized to the incident light in absence of scattering structures obtained in a second computation to obtain a spectrum.

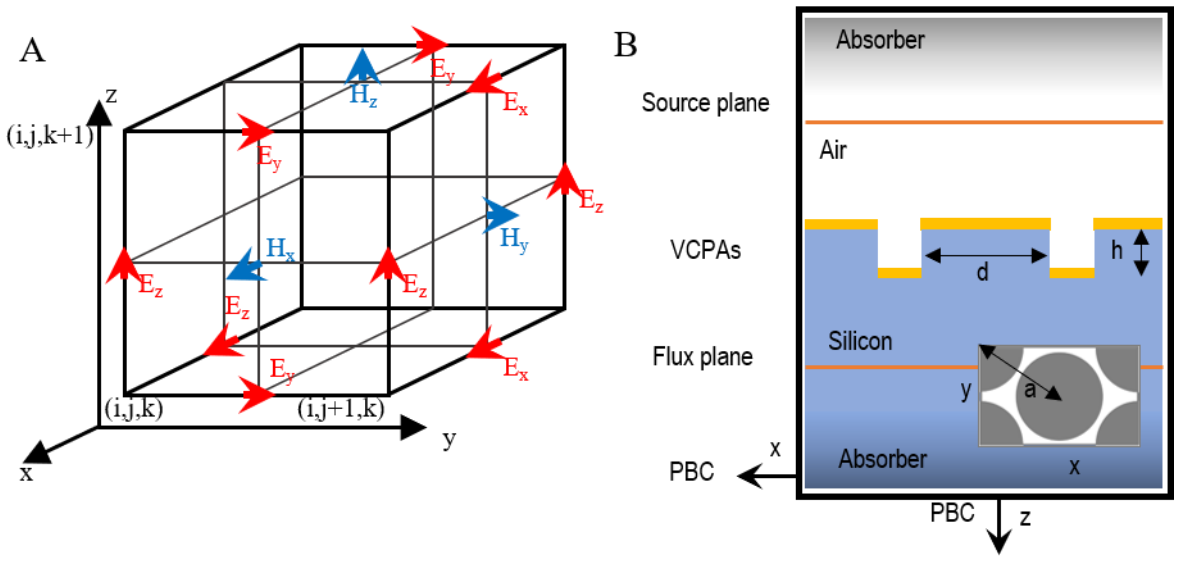

Figure 3.3 (A) Yee cell used in FDTD simulations. Electric and magnetic field components are separated by half a pixel. (B) Cross section of the simulation cell. The cell is bloch-periodic in all dimensions. An absorber layer hinders the transmission out of the cell perpendicular to the source.

In general, materials are described in the FDTD algorithm with the Lorentz-Drude model. The Drude model is only an accurate description for the optical response before electronic interband transition start to occur which start for some noble metals already at 1 eV (corresponding to $\lambda \sim 1\ \mu m$)[51]. These transitions can be described with Lorentz-oscillators in the form of $\frac{A_f}{\omega_f^2-\omega^2-i\omega\gamma}$ where A_f is the corresponding oscillator strength, ω_f the resonance frequency and γ the electron scattering rate due to lattice imperfections (phonons or defects). For $\omega_f = 0$, neglecting damping losses and $\sqrt{A_f} = \omega_p$ one obtains the well-known Drude Term $\epsilon(\omega) = 1 - \frac{\omega_p^2}{\omega^2}$. The complete dielectric function of a material is then the sum over all oscillators:

$$\epsilon(\omega) = 1 + \sum_{f=1}^{M} \frac{A_f}{\omega_f^2 - \omega^2 - i\omega\gamma} \tag{3.12}$$

The material constant for gold and other metals were described by experimental data obtained from Rakić et al. [67] and implemented into the *Meep* script. Dielectric materials were on the other hand described dispersionless with a constant refractive index.

3.4 Vertically coupled plasmonic arrays in the Infrared

Complementary vertically coupled plasmonic arrays (VCPAs) were first studied by Li et al.[12]. In general, these VCPAs have a structure that can be described as two displaced, complementary plasmonic slabs. These plasmonic slabs consist of (*i*) a plasmon active metal film with submicron sized and periodically ordered perforations, and (*ii*) complementary, periodically ordered plasmon active antennas (see fig. 1.1). Typically, the size and shape of the discs are exactly complementary to the voids in the perforated film, though there exist examples of not strictly complementary VCPAs [68, 69]. The geometrical dimensions of these systems dictate and enable a designed complex optical response. Whereas the displacement of the two slabs determines their coupling strength, the resonance is also greatly influenced by the perforation size and shape, the array period (pitch), as well as by array symmetry. Matching the geometric dimensions carefully, a spectral window of extraordinarily optical transmission (EOT) can be engineered [70-73]. The effect is based on the fundamental surface plasmon excitation of periodically perforated thin metal films [70].

Recently Akinogu et. al [6] has investigated the plasmon resonance of VCPAs in the mid-infrared regime (see fig. 3.4(A)). In that region the plasmon region is retarded and the plasmon dispersion approaches the light line (see fig. 3.4(A)). It was shown that plasmon resonance is linearly

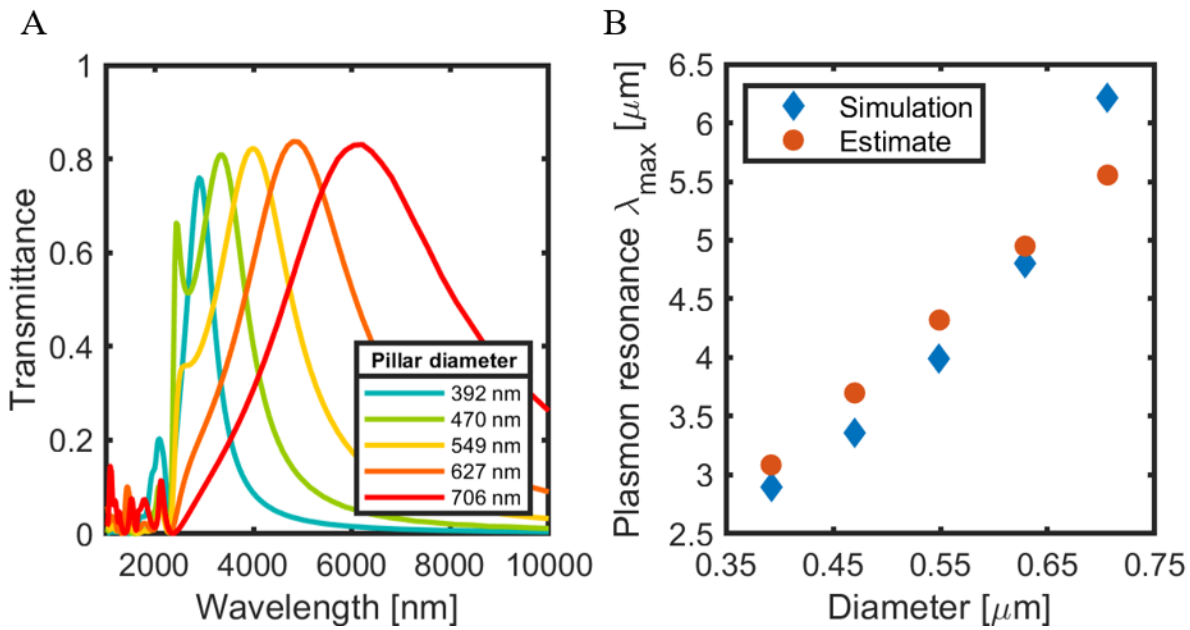

Figure 3.4 (A) Transmittance spectra for different pillar diameters, and fixed height = 200 nm and pitch = 784 nm. (B) Comparison between simulated and estimated plasmon resonance position. Adopted from Ref. [6].

dependent on the diameter and the plasmons can be interpreted as whispering gallery modes in the form (fig. 5(B)):

$$\lambda_{pl} = \pi d\sqrt{\varepsilon} \tag{3.13}$$

where d is the pillar diameter and the background dielectric constant is $\epsilon \approx (1 + \epsilon_{Substrate}) / 2$. Accordingly, the plasmon mode circulates around the circumference of the disk/hole. Equation 3.13 also implies that the excitation energy is independent of the plasmonic material (because the plasmon dispersion follows the light line). In the next chapter the plasmonic resonance of VCPAs is computational investigated in a regime in which block copolymer lithography can be employed and where the plasmon resonance is non-retarded and becomes strongly material dependent.

4. Materials design of vertically coupled plasmonic arrays

The cost effective fabrication of nanopillar templates by nanoimprint lithography[74, 75], roll-to-roll nanoimprint processing[76, 77], block copolymer lithography[78] and hot embossing/nanoinjection moulding[77, 79] enable an effective route to create plasmonic metasurfaces on an industrial scale. Subsequently, a thin metal coating can simply be deposited onto the nanopillar template to create a plasmonic slab that consists of a perforated film comprised out of a hole array at the base of the nanopillars and a quasi-Babinet complementary disk array on top of the nanopillars. The plasmonic properties of the template can be adjusted by the choice of metal and support material and the geometrical dimensions of the underlying structures[6]. For small nanopillar aspect ratios the plasmon resonance of (*i*) the disk array and (*ii*) the hole array can hybridize and couple vertically. The optical response of such vertically coupled plasmonic arrays (VCPA) exhibits extraordinary optical transmission which has been exploited to fabricate optical filters[71, 80, 81], refractive index sensors[82-84] or plasmonic nanopixels beyond the diffraction limit[4, 85, 86]. Further, small plasmonic junctions between the two plasmonic slabs of the VCPAs can drastically increase the local electric near-field. This effect has been used to increase sensitivity of spectroscopic instrumentation such as in surface-enhanced fluorescence spectroscopy[87, 88] , surface-enhanced Raman spectroscopy[12, 78] and surface-enhanced infrared spectroscopy [13].

Previously, it has been shown that the plasmon resonance of VCPAs with hexagonal symmetry can be described as whispering gallery modes in the mid-infrared[6]. In this regime the plasmon resonance is retarded and the plasmon dispersion follows the light line[50, 89]. As a consequence, the plasmon resonance is independent of the plasmonic material as long as the material is conductive[90]. This drastically changes in the visible region of the electromagnetic spectrum where

the plasmon resonance is non-retarded and deviates from the light line[50, 89]. In this regime the plasmon resonance is governed by Mie resonances, which are highly material dependent[50, 90].

The choice of the metal employed in the VCPAs is often specific to the intended application, where in addition to the metal's plasmonic properties, other aspects such as its abundance, stability to oxidation, biological compatibility, magneto-optical properties, and catalytic activity are important. Gold and silver are the most commonly employed plasmonic metals due to their excellent plasmon activity and stability, however they are expensive. Copper and aluminum are readily available but oxidize when in contact with air. A protective polymer coating can hinder this oxidation, however this blocks access to the metal surface where the plasmonic field is at its strongest. Nickel and palladium have received wide attention for their catalytic capabilities, but as plasmonic materials they face challenges such as high loss, and high expense, respectively. Here, a comprehensive overview of the optical properties of VCPAs consisting of various plasmonic materials, dielectric supports, and geometrical dimensions, as simulated by finite-difference time-domain (FDTD) simulations, is provided. Such simulations are routinely used to predict and verify the optical behavior of experimentally fabricated plasmonic metasurfaces[4, 6, 12, 13, 50, 71, 74-89]. Finally, it is demonstrated that VCPAs can effectively form plasmonic hetero structures commonly used in plasmon enhanced photocatalysis.

4.1 Quasi-Babinet complementarity

Babinet's principle states that the transmittance T_λ of a slab and the transmittance of its complementary counterpart $T_{\lambda,c}$ is related as:

$$T_\lambda + T_{\lambda,c} = 1 \tag{4.1}$$

The principle assumes that the film thickness is infinitesimally small and does not account for absorption losses or coupling effects. Equation 4.1 implies that the plasmon excitation energy of a disk array and that of its complementary hole array should be identical. In Figure 4.1(A) the transmittance of hexagonally-arranged Au nanodisks on glass nanopillars with varying diameter were simulated. The plasmon resonances show a large dip in the region between 515 nm and 630 nm, exhibiting a slight red shift with increasing particle size. The shift can be explained by the lower restoring force experienced be the opposing charges as the size increased resulting in a lower excitation energy of the localized surface plasmon.[26] In the long wavelength limit the transmission approaches 100 percent and in the short wavelength limit the slab shows reduced transmission due to the intrinsic absorption of Au, which scales with the fraction of Au covering the surface. In Figure 4.1B the transmittance of quasi-Babinet complementary perforated film at the base of the nanopillars is shown. The spectra reveal extraordinary transmission (EOT)[70] with peaks that are slightly red-shifted relative to their quasi-Babinet complementary counterparts in Figure 4.1(A) . The slight red shift is attributed to the increased polarizability of the immediate environment of the perforated films because is buried inside the nanopillar template as in contrast to the disks which are on top of the pillars. Nevertheless, equation 4.1holds qualitatively.

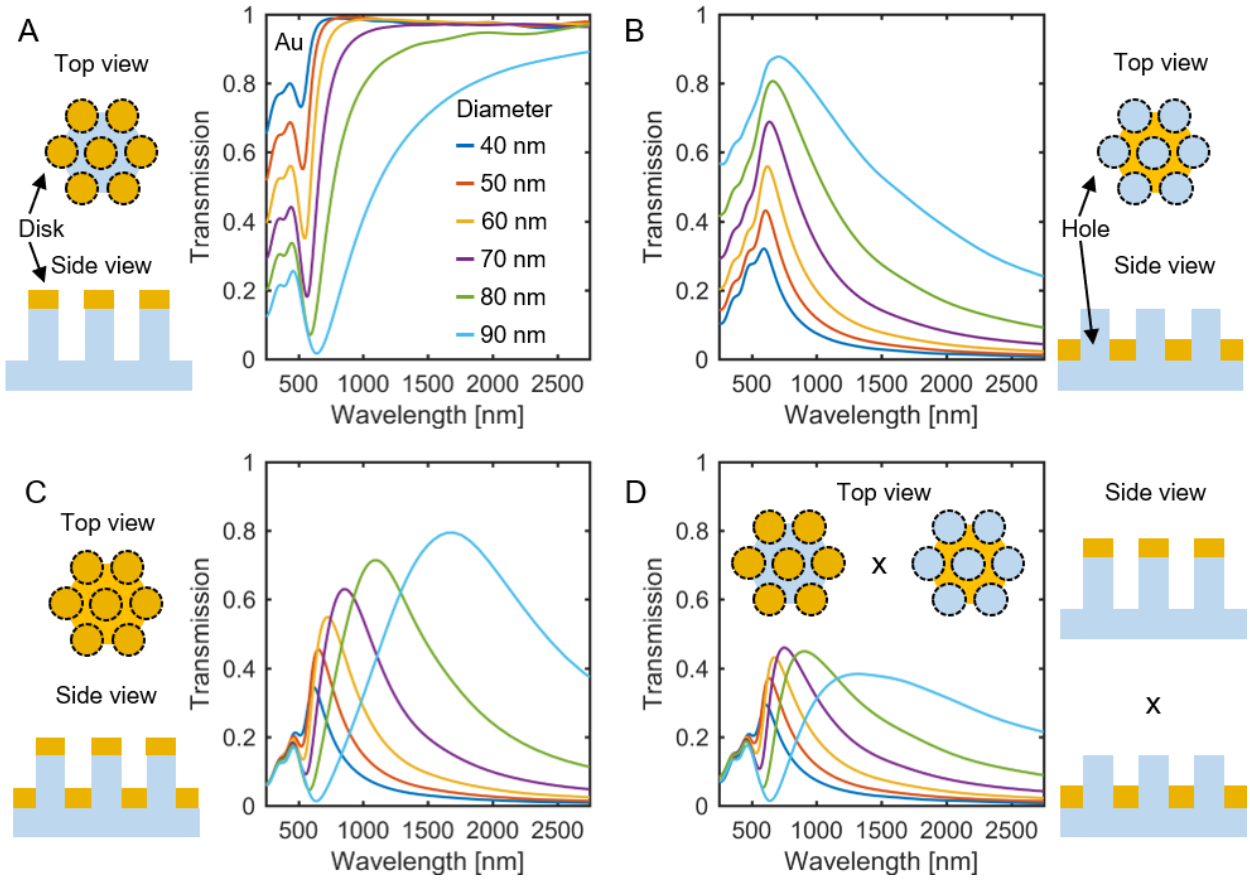

Figure 4.1 FDTD transmittance spectra of periodic plasmonic gold arrays on a nanopillar support with varying diameter and fixed height = 70 nm, pitch = 100 nm and gold thickness = 40 nm. The drawings on the sides show the simulated structures. (A) Nanopillar array with gold disks on top of the pillars. (B) Nanopillar array with hole array at the base of the pillars. (C) VCPAs; nanopillar arrays with gold disks on top of the pillars and hole array at the base of the pillars. (D) Multiplication of the respective spectra from (A) and (B).

In Figure 4.1(C) the corresponding VCPAs with the presence of both the Au disk and hole array slabs together are shown. The EOT peak is highly symmetric, red-shifts and increases in transmission with pillar diameter. To understand the origin of this behavior, the respective disk and hole array spectra from Figure 4.1(A) and Figure 4.1(B) were multiplied, assuming that $T_{total} = T_{Disk}T_{Hole}$ (see Figure 4.1(D)). The multiplied spectra show an impressive qualitative agreement with those in Figure 4.1(C), exhibiting EOT and a diameter dependent red-shift, underscoring the power of Babinet's principle. However, this simple approach ignores the fact that the pillars

are 70 nm in height and therefore the complementary plasmonic arrays are in each other's near-field such that their plasmonic modes can hybridize[91]. Further, the VCPAs, show a reduced spectral energy width compared to the perforated film which is an important design factor for narrow bandpass filters (Figure S1(in the appendix)) shows the spectra in Figure 1 vs eV instead of wavelength)[92].

4.2 Pitch, vertical gap and metal thickness

The results in Figure 1 have shown that the pillar diameter is a significant parameter of the plasmon excitation energy of VCPA's. The variation of the other geometric parameters is investigated here. In Figure 11, the effects of the pillar height (Figure 4.2(A)), the metal film thickness at a constant 5 nm vertical gap between the hole array and the disk array (Figure 4.2(B)), and the pillar separation, i.e. the array pitch (Figure 4.2(C)), on the optical response of the VCPAs are shown. The results show a slight red shift of the VCPA EOT peak for shorter pillar heights and smaller array pitch. This is in agreement with the plasmon hybridization model, which predicts for the bonding modes a red shift for decreasing plasmonic gaps[91]. The absorption spectra reveal two absorption modes at 525 nm and at 670 nm for a 5 nm vertical gap. The two peaks blue-shift for larger pillar heights, where the lower energetic mode experiences a larger shift. Eventually the two peaks overlap for larger gaps. Moreover, the electric-near fields were plotted as a function of the wavelength. The respective electric near-field maxima with frequency ω_{NF} occur at lower excitation frequency than the respective far-field absorption at frequency ω_{FF}. The phenomenon can simply be explained by a driven and damped harmonic oscillator model and directly depends on the total damping (radiative plus intrinsic) γ of the system [93]. Precisely, the equation reads $\omega_{NF} = \sqrt{\omega_{FF}^2 - \gamma/2}$ [93]. The shift between near- and far field response for traditional plasmonic materials in the visible spectral

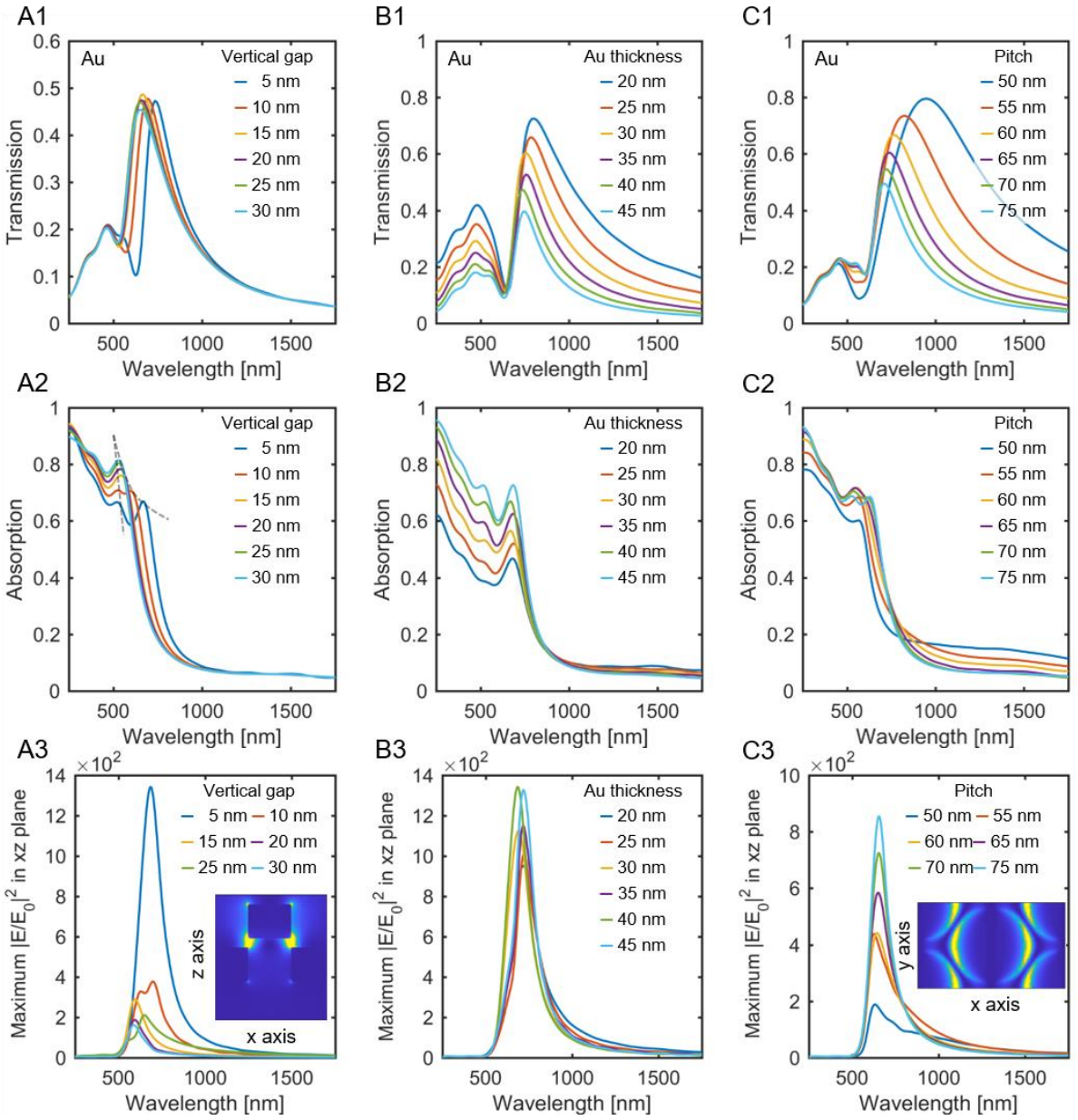

Figure 4.2 Au based VCPAs. (A) Variation of the vertical gap (pillar height) with fixed pitch = 100 nm, diameter = 50 nm and Au thickness = 40 nm. (A1) Transmission spectra, (A2) absorption spectra where the grey dashed lines provide a guide for the eye for the shift of the two modes, and (A3) electric near-field enhancement. The inset shows the cross-section map at the, the plasmon resonance for a 10 nm vertical gap between the disks and holes for x-axis polarization. (B) Variation of the Au thickness (pillar height) with fixed pitch = 100 nm, diameter = 50 nm and vertical plasmonic gap = 5 nm. (B1) Transmission spectra, (B2) absorption spectra and (B3) electric near-field enhancement. (C) Variation of the pitch with fixed height = 45 nm, diameter = 40 nm and Au thickness = 40 nm. (C1) Transmission spectra, (C2) absorption spectra and (C3) electric near-field enhancement. The inset shows the in-plane map 1 nm above the perforated film at plasmon resonance for a 10 nm lateral gap between the holes for x-axis polarization.

region is in the order of up to ~100 nm[94]. The near-field spectra reveal a strong vertical coupling between the disk array and the hole array, which is largest for the smallest vertical gap. The Au thickness on the other hand has only a small effect on the plasmonic response. An increase in the metal thickness shows a slight blue shift in the resonance position, because the polarizability of the material increases[95]. The variation of the pitch shows a strong red shift for the pitch approaching the size of the nanopillar diameter, i.e. smaller lateral gap. However, the electric near-field enhancement does profit from the lateral coupling, Contrary, the electric near-field reduces for smaller pitches.

4.3 Plasmonic metal

The choice of the metal strongly determines the plasmonic response in the non-retarded regime. Different metals have a different bulk plasma frequency, which depends on the density *N* of free charge carriers.

$$\omega_p = \sqrt{\frac{Ne^2}{\varepsilon_0 m_e}} \tag{4.2}$$

Where m_e is the effective electron mass and ε_0 is the free space permittivity. In addition, damping caused by inter-band or intra-band transitions influences the plasmon position and strength[93, 96]. For many metals intra-band transitions are a threshold, where all incident photons with larger energies will excite electron-hole pairs and reduce the plasmonic response. For Au the threshold is at ~ 515 nm, for Ag at ~ 310 nm and for Cu at ~ 575 nm. An exception is Al which has an intra-band transition that is spectrally localized around λ = 800 nm and which enables Al to remain plasmon active in the UV[30]. The transmittance of VCPAs for different metals as a function of pillar diameter is shown in Figure 12. Au (Figure 4.3(A)), Ag (Figure

4.3(B)) and Cu (Figure 4.3(C)) have a similar far-field response owning to their similar intrinsic properties. Ag also shows a small EOT peak in the UV, where Au and Cu are not plasmon active. The Al plasmon reosnance is significantly blue shifted compared to the other metals due to its large bulk plasma frequency, which is roughly 5 eV higher than that of Au with $\omega_{p,Au}$~9 eV (Figure 4.3(D)). The transmisison spectra show that the EOT peak has a dip caused by the localized intraband transition of Al. For

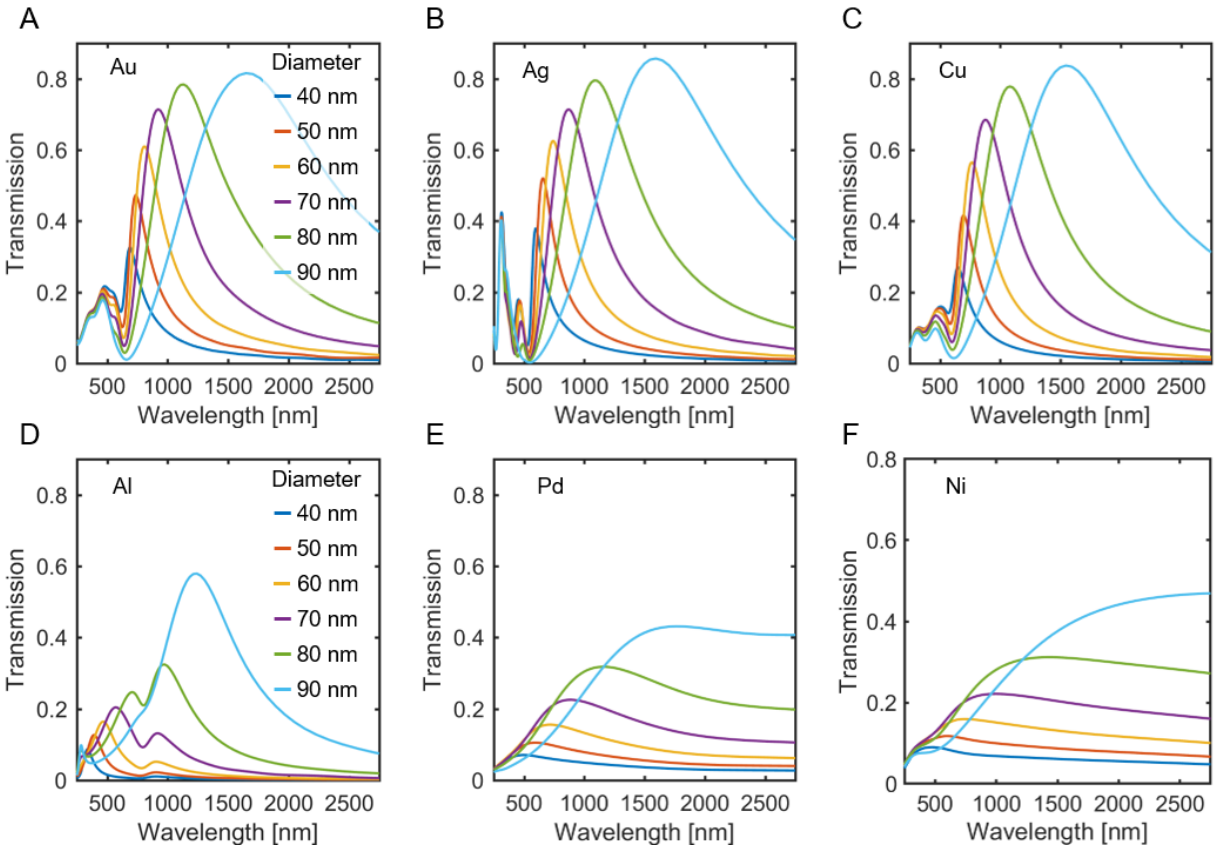

Figure 4.3 FDTD transmittance spectra of VCPAs with varying diameter, fixed height = 45 nm and fixed pitch = 100 nm for different metals. (A) Au, (B) Ag, (C) Cu, (D) Al, (E) Pd and (F) Ni.

large diameters it vanishes in flanks of the EOT peaks. Pd and Ni have a broad and weak EOT peak, which stretches deep into the near infrared caused by their large damping factors (Figure 4.3 (E) and Figure 4.3(F)).[95, 96]

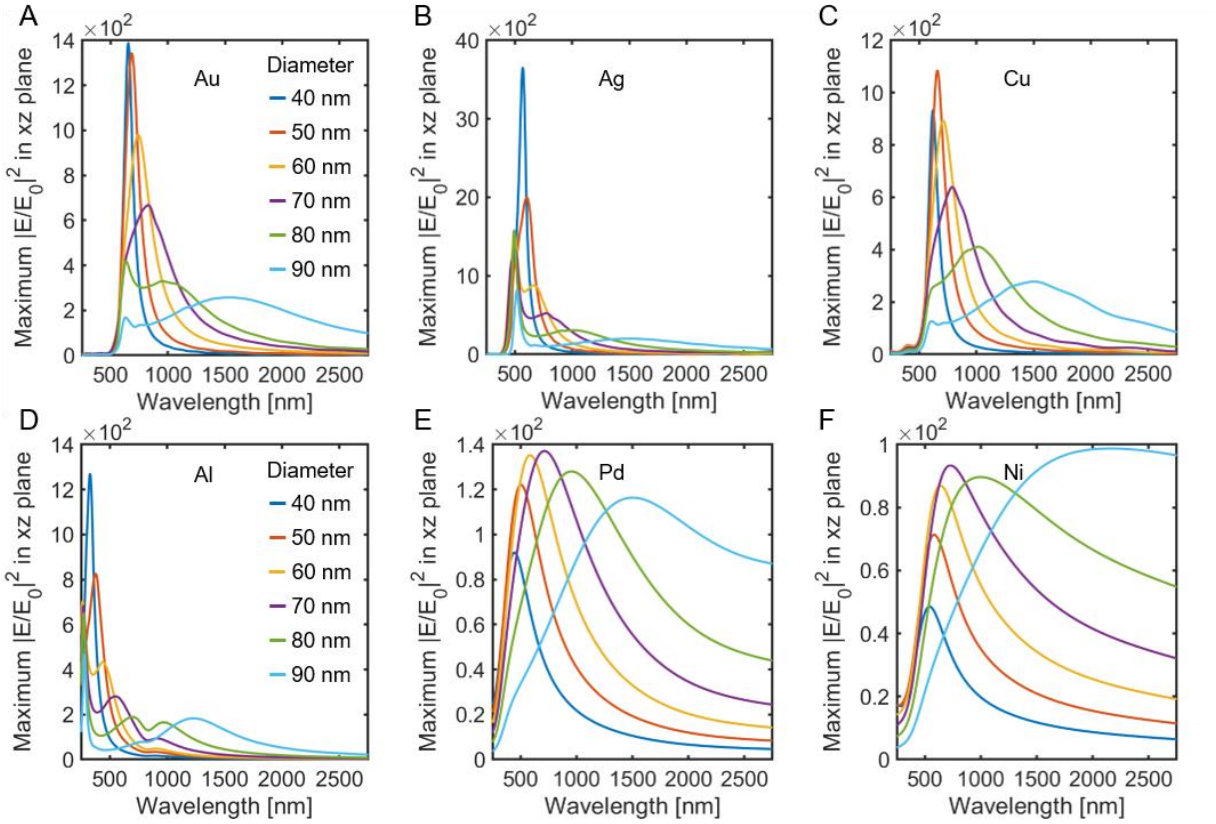

Figure 4.4 Simulated electric near-field enhancement of VCPAs at the cross-section plane with varying diameter and fixed height = 45 nm and fixed pitch = 100 nm for different metals. (A) Au, (B) Ag, (C) Cu, (D) Al, (E) Pd and (F) Ni.

The electric-near field spectra reveal that traditional plasmonic materials have a larger maximum enhancement factor for smaller disk/hole diameters (Figure 4.4(A-D)). For short pillar diameters the two previous observed modes overlap and split up for larger diameters. However, the high energetic mode only exhibits a small shift compared to the other lower energetic mode. For larger diameters, a broader but weaker peak appears that corresponds to the plasmonic

bonding mode. Ag shows the strongest near-field enhancement which is in agreement with experimental surface enhanced Raman studies[97]. Pd and Ni feature significantly smaller near-field enhancement which is caused by their large damping factors (Figure 4.4 (E) and Figure 4.4(F)).

4.4 Dielectric support

The plasmon resonance position is extremely sensitive to the dielectric environment of plasmonic nanostructure [82-84]. This property is extensively used in surface plasmon resonance spectroscopy to detect binding events of biological macromolecules at the plasmonic template[84]. Therefore, the refractive index of the substrate and the pillars is important. Here VCPAs with pillars made from different optically transparent substrate materials are investigated with substrate material refractive indices ranging from 1.46 to 2.60. In Figure 4.5(A) and Figure 4.5(D) the effect is shown for Au-based VCPAs for the far- and near-field. The plasmon resonance red shifts with increasing refractive index. The line width and EOT maxima however are not significantly altered. The other metals show a similar behavior with a linear dependence on the refractive index (Figure 4.5 (B)). The slopes for Pd and Ni are slightly steeper than for the other metals. The difference is attributed to their broader EOT maxima. The transmission maxima at the EOT position do not show a strong variation with refractive index for any of the considered metals (Figure 4.5 (C)). Fresnel reflection coefficients predict a five times higher reflection from an air-titanium dioxide interface than for an air-glass interface. However, the EOT doesn't show a significant variation for different refractive indices which, illustrates a fundamental difference in the light-matter interaction based on the plasmonic activity.

Next, the effect of the substrate material on the VCPA near-field properties is examined. The near-field resonance exhibits a linear excitation wavelength dependency for all the metals with similar slopes. Previously is was observed that the optical near-field could be reduced more than

three times for planar plasmonic templates on a high refractive substrate materials (n_{Si}=3.4) as compared to a low refractive index substrate (n_{CaF2}=1.3)[98]. It was suggested that placing plasmonic templates on nano-pedestals could overcome the electric screening by the substrate[99, 100]. However, our results indicate that the maximum electric near-field enhancement for VCPAs remain the same or is only slightly decrease for larger refractive index pillars (Figure 4.5 (F)). Furthermore, for Cu a slight increase is observed. Therefore, it is concluded that the vertical plasmonic coupling alongside the air-substrate interface is robust towards substrate effects.

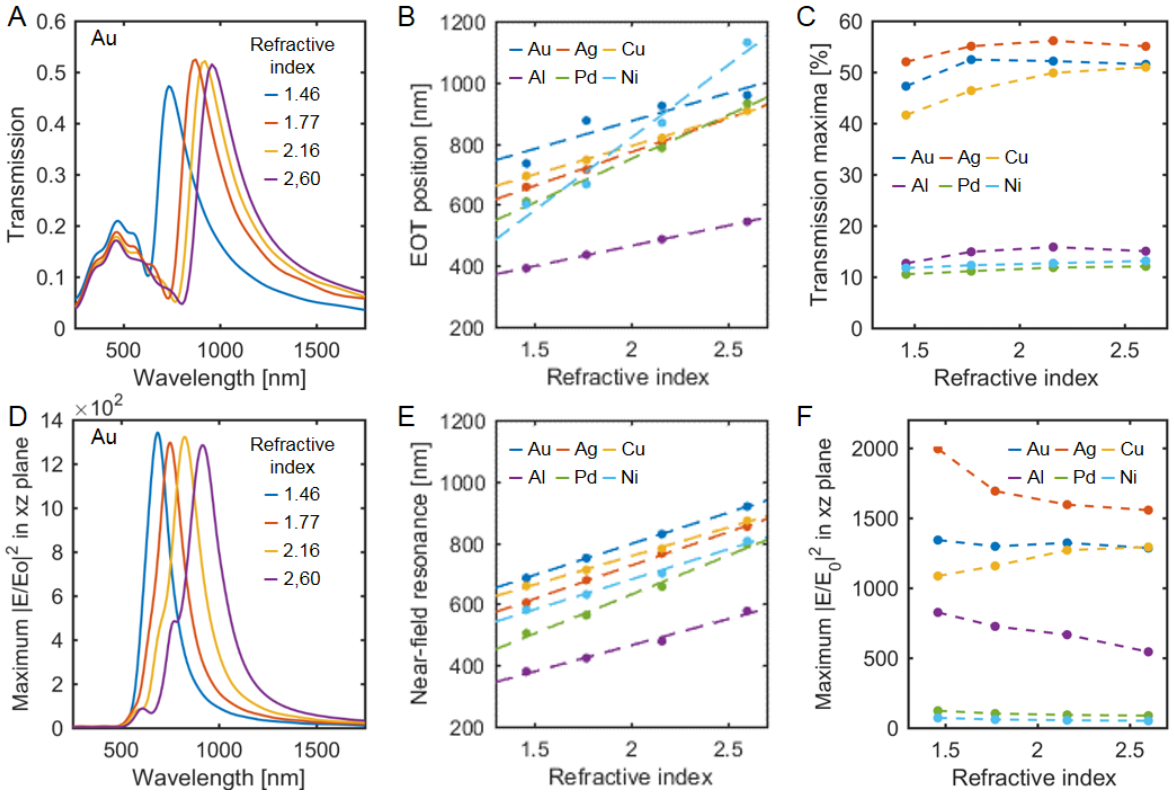

Figure 4.5 VCPAs with variation of the nanopillar materials and corresponding refractive index. The materials probed are glass (n=1.46), sapphire (n=1.77), cubic zirconia (n=2.16) and titanium dioxide (n=2.6). (A) Au transmission spectra. (B) Change of the EOT peak position for different metals depending on the refractive index. (C) Respective maximum transmission value depending on the refractive index. (D) Electric near-field enhancement of Au. (E) Electric near-field resonance position for different metals versus the refractive index of the nanopillars. (F) Maximum electric near-field enhancement depending on the

4.5 Plasmonic heterostructures

A promising strategy to increase the efficiency of conventional catalysts is to combine them with strong plasmonic metals[101, 102]. This can be either a core shell or bilayer configuration where the catalytic system consists of two or more different metals. Alternatively, the antenna-reactor geometry consists of a plasmonic antenna, which is excited optically and then transfers the energy to a proximal catalytic reaction site to facilitates a chemical reaction[103]. The VCPAs provide a simple route to combine both these strategies by sequentially depositing two different metals on a nanopillar template. Ideally, the catalytic system should fully absorb light over a broad spectrum. The plasmon decay generate hot charge carriers that can subsequently participate in chemical reactions. It has also been reported that some reactions are even directly driven by strong electric near-fields[104]. To explore the potential of bimetallic VCPA as plasmonic two different series were simulated. First, we consider a situation where the nanopillars are coated first with Pd and then with Ag on top (Figure 4.6(A-C)). Figure 4.6A shows that the heterostructure shows a strong vertical coupling between the Pd disks and the perforated Ag film. Absorption spectra reveal that the smaller diameter VCPAs can absorb up to 90% of the light (Figure 4.6(B)) similar to the pure Pd VCPA counterpart. The electric near-field enhancement shows a more than one order of magnitude higher enhancement than for the pure Pd VCPAs which proves the superiority of the heterostructures (Figure 4.6(C)). In the second situation the reverse geometry is considered, i.e. Pd is deposited on top of silver (Figure 4.6(D-E)). Here, the

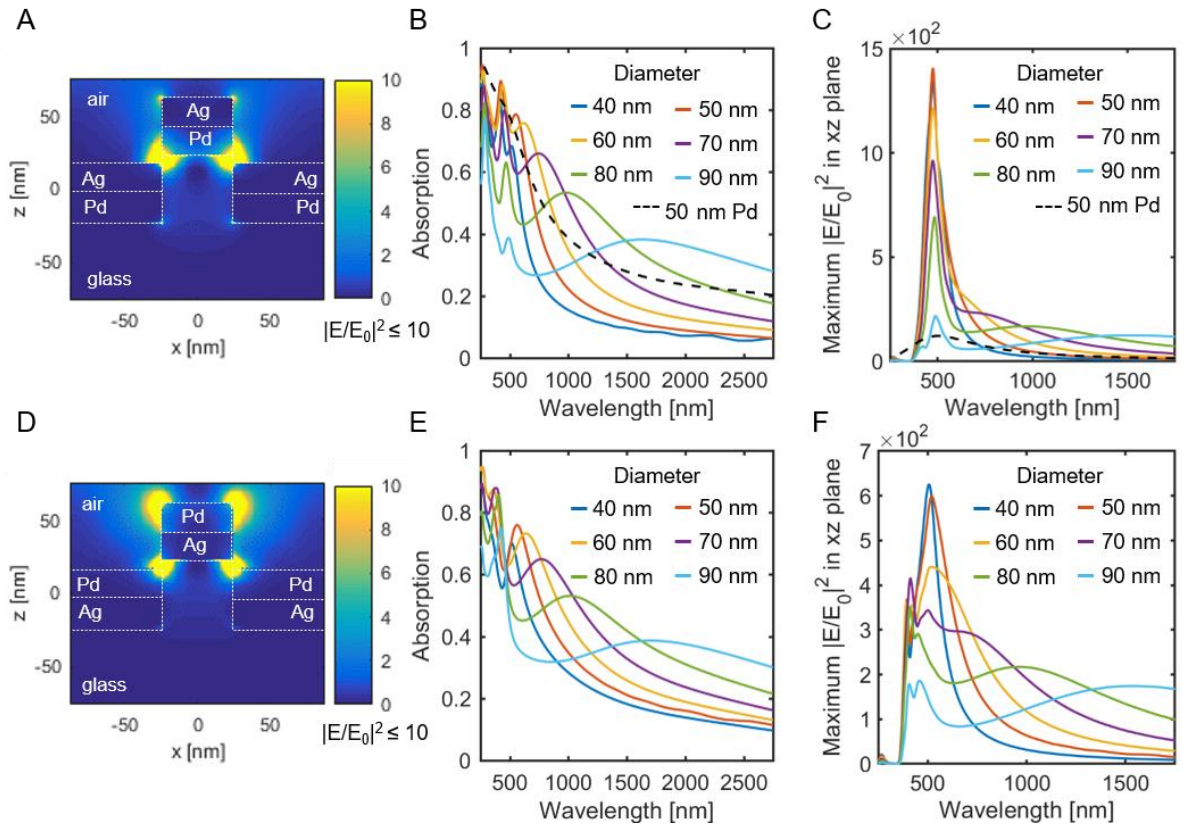

Figure 4.6 Metallic bilayers on glass nanopillars with pitch =100 nm, metal thickness = 40 mn and pillar height 45 nm. (A-C) Ag on top of Pd. (A) Cross section with 50 nm diameter. (B) Absorption spectra and (C) electric near-field enhancement with varying diameter. The black dotted line is the respective spectra for pure Pd and 50 nm diameter size. (D-F) Pd on top of Ag. (D) Cross section with 50 nm diameter. (E) Absorption spectra and (F) electric near-field enhancement with varying diameter.

plasmonic slabs shows strong coupling between the perforated Pd film and the silver disks (Fig. 4.6(D)). Additionally, the Pd discs also show a strong electric near-field enhancement. The overall light absorption is similar to the first case where Ag was placed on top of Pd but the electric-near field enhancement is reduced by ½. However, for catalytic application, it is more feasible to place the Pd on top of Ag because in this configuration the surface area of the catalytically active Pd greatly larger.

4.6 Conclusion

The plasmonic response of vertically coupled plasmonic arrays (VCPA) is dominated by the extraordinary optical transmission (EOT) effect, which can be tuned by the geometrical parameters. The diameter of the disks/holes has the largest influence on the resonance position. The EOT maxima red shifts for decreasing lateral and vertical plasmonic gap sizes. The near-field maxima correspond to the anti-bonding mode which correspond to the transmission minima. The best electric near-field enhancements are observed for short vertical gaps and large lateral gaps. Ag showed superior near-field enhancement compared to the other metals. The plasmon resonance of Pd and Ni VCPAs show only a weak and broad EOT response and small electric near-field enhancements. The resonance of Al is considerably blue shifted as compared to the other metals. The variation of refractive index of the nanopillar shows a small linear dependence on the linewidth, near-field enhancement and absolute EOT resonance position . Ag-Pd heterostructures were considered for plasmon driven catalytic applications and exhibit light absorption up to 90% and superior electric near-field enhancements compared to pure Pd VCPAs. Concluding, the derived principle mechanism of the plasmonic response of VCPAs are in the next chapter used to design a surface enhanced Raman template with block copolymer lithography.

5. Vertically coupled plasmonic arrays for Surface Enhanced Raman Spectroscopy

Surface Enhanced Raman Spectroscopy (SERS) is a versatile tool for the detection of analytes in ultra-small concentrations. It gives valuable information about molecular vibrations in the vicinity of plasmon active surfaces[18]. It is widely accepted that the main mechanism of the Raman scattering enhancement is the large local electric field amplification at sharp edges or at nano-meter sized gaps between plasmonic particles, so called electromagnetic hot spots[18]. In the last decade, much effort has been concentrated on the fabrication of economically viable SERS sensors with a high density of effective hot spots[18]. The fabrication approaches can be separated into bottom-up and top-down methodologies. Bottom-up approaches consist of metallic colloids such as nanoshells[105], nanorods[106] and nanostars[107] prepared by wet chemistry. Their preparation is easy, scalable and cost effective while also providing a strong SERS enhancement. Though, the lack of precise control over the nanoparticles shape, size and arrangement result in different Raman intensities and reproducibility is still a challenge[18]. Top-down approaches are generally based on lithographic fabrication methods with higher control of the SERS substrate geometrical parameters. However, this incurs higher costs and lower throughput. Lithographic based SERS substrates typically consist of metallic dot arrays and their complementary perforated thin films[108]. In recent years, much attention has focused on the study of nanopillar arrays whose top and base are coated by metals, enabling large SERS enhancement factors and increased surface area[109]. This approach allows recycling of the plasmon active layer deposited on the nanopillars once it is contaminated[110]. The perforated metal film at the base of the array can also be used as an electrode for (spectro-)electrochemistry[111]. Many methods have been presented for the fabrication of nanopillar arrays for SERS application including maskless

reactive ion etching [16, 112, 113], nanosphere lithography[114, 115], laser interference lithography [116], E-beam lithography [10, 17, 117] nanoimprint lithography[12, 118] and block copolymer lithography[110, 119].

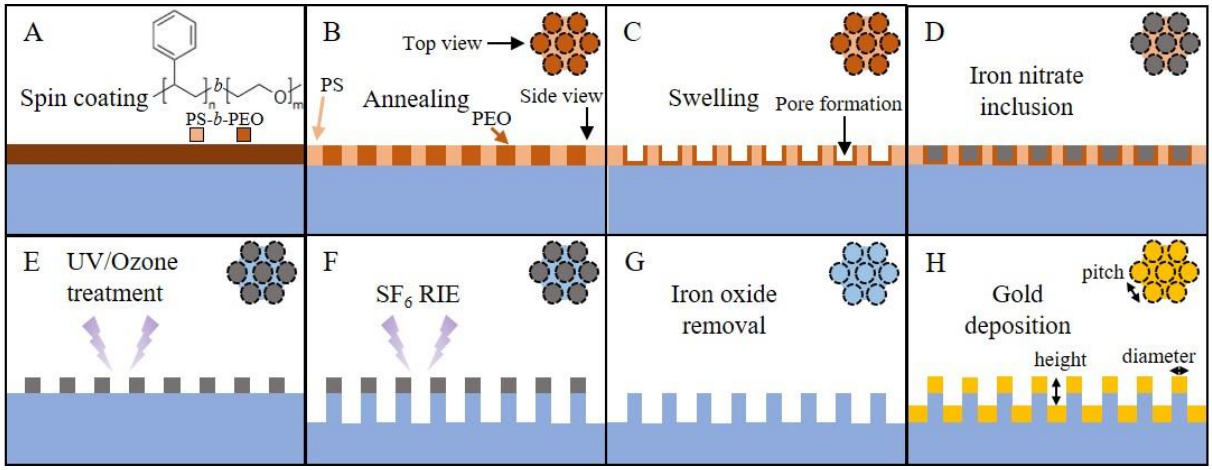

Figure 5.1 Fabrication process: (A) The block copolymer is spin cast on silicon, (B) microphase separation of the BCP by solving annealing and (C) ethanol swelling of the phase separated film. (D) Incorporation of iron salt into the BCP film, (E) polymer removal, and the formation of iron oxide nanodots by UV/ozone treatment. (F) Iron oxide nanodots are used as an etch mask, (G) the iron oxide is removed from the top of the pillars and (H) Gold is deposited and VCPAs are obtained.

A common strategy is based on pillar arrays with large aspect ratios in the order of 10:1. After a target analyte is drop coated on the SERS substrate and on subsequent solvent evaporation, the pillars aggregate due to surface tension. The result is a strong lateral coupling of the plasmon- active metals deposited on top of the pillars, which deliver a strong SERS enhancement [16, 110, 112-114, 119]. In addition, hydrophobic pillar arrays can confine the spread of droplets and consequently increase the analytes concentration at the initial impact area of the droplet on the SERS substrate[120]. However, the aggregation based strategy leads to non-uniform local Raman intensities that can vary up to a factor 2 across the substrate[110]. It is also disadvantageous for *in-*

situ studies in aqueous environment and for analytes that require a controlled functionalisation of the gold surface[121].

As an alternative approach pillar arrays with a small height-to-diameter aspect ratios can be used [10, 12, 17, 117, 122]. These nanopillars enable two types of coupling depending on their geometrical parameters: (i) Lateral coupling in between the top of the pillars [122], (ii) or vertical coupling of the metal layers deposited on top of the nanopillars and dewetted gold clusters on the side wall of the nanopillars that typically arise from an inhomogeneous metal deposition process[10, 12, 17, 117]. Here, SERS substrates fabricated by block copolymer lithography and based on strong vertically coupled plasmonic arrays (VCPAs) between the gold layer on top of the nanopillars and a perforated gold thin film at their base is presented. It is demonstrated that the Raman intensity drastically increases for decreasing gap sizes between the perforated film and the disk array. Previous nanopillar SERS substrate fabricated by block copolymers relied on a costly atomic layer deposition intermediate step [110, 119]. Such arrays can be fabricated by a novel cost effective and scalable process based on the selective incorporation of iron precursors in microphase-separated block copolymer films to form an etch mask[20] (see fig. 5.1).

5.1 Sample fabrication

The optical properties and the SERS enhancement of the VCPAs is governed by the geometrical parameters of the plasmonic slab [12, 71]. The best enhancement is achieved when the plasmon resonance is tuned to the laser excitation wavelength. Tuning can be made by adjusting the pillar height through the etching process parameters. The pitch and pillar diameter are defined by the initial etch mask predefined by the block copolymer system. The relative size and structure of the block copolymer film can be varied through altering the molecular weight, volume fraction

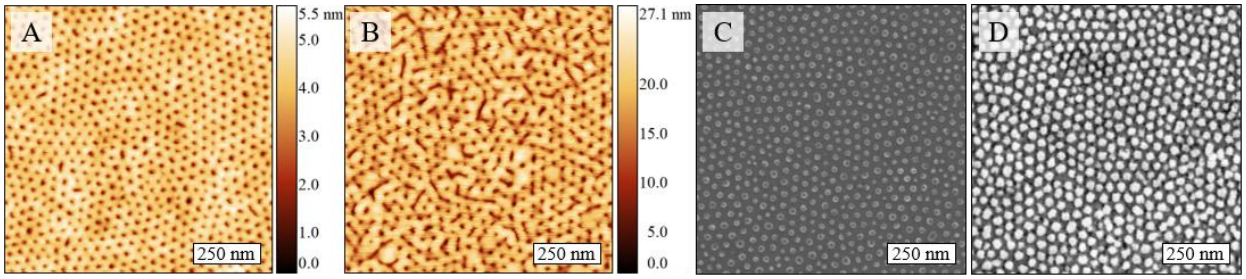

Figure 5.2 Fabrication process steps: (A) AFM image after phase separation of PS-*b*-PEO, (B) swelling of the block copolymer film (C) Top down SEM image of iron oxide dots hard etch mask transferred onto the silicon substrate after polymer removal and (D) of VCPAs.

and chemical structure of the components of the block copolymer. Here polystyrene-*b*-poly(ethylene oxide) (PS-*b*-PEO) block copolymer was used with respective average molecular masses of blocks M_{PS}=42 kg mol^{-1} and M_{PEO}=11.5 kg mol^{-1} [123, 124]. The block copolymer system has been previously well studied and the derived pattern show large scale uniformity which has been confirmed by grazing-incidence small-angle X-ray scattering[45, 46]. A 1 wt/% block copolymer solution in toluene was spun cast onto a silicon substrate for 30 seconds at 3000 rpm, which was followed by solvent vapour annealing in a glass jar in toluene atmosphere for 80 minutes at 50 °C. Thermal solvent annealing facilitates the mobility of the polymer chains so that the cast film can restructure into a more stable state in thermal equilibrium. As a result, the block copolymer phase separates into hexagonal ordered PEO domains in a PS matrix, observed by AFM analysis (Figure 5.2(A) and a corresponding AFM profile line in figure S2 (in the appendix)). Next, the phase-separated film is swelled in anhydrous ethanol for 14 hours and at 40 °C to expand the depth of the domains from 6 nm to up to 27 nm (Figure 5.2(B) and a corresponding AFM profile line in figure S3).

The increased dimensions of the pores enable the incorporation of larger volumes of the final etch resist into the polymer domains. Adding this resist is essential, because the selectivity of

the polymer etch mask is low compared to conventional etch masks[20]. Therefore, freshly prepared 0.4 wt% iron (III) nitrate solution in anhydrous ethanol was spun cast (30s, 3000 rpm) on the substrate to fill the PEO pores. The polymer organics are removed by 3 hours UV/ozone exposure, while also oxidizing the iron inside the cavities[46]. The fabricated iron oxide arrays have an average dot diameter of d = 28.4 nm ± 4.4 nm and a pitch of a = 42.3 *nm* ± 3 *nm* (Figure 5.2(C) and diameter and pitch histograms in figure S4 and S5 and an AFM analysis in figure S6). A small pitch compared to the diameter is favourable because it increases the pillar density and therefore hot-spot formation for SERS. It also results in lateral coupling between the apexes of the pillars. The nanopillars are created by reactive ion etching in a fluorinated plasma, where the pillar height is well controlled by adjusting the etch duration (see figure S7 for SEM top down views with different magnifications). To prevent cross-contamination of the SERS spectra due to carbon fluoride, the silicon etching is followed by an oxygenated plasma-cleaning step. Finally, any remaining iron oxide dots are removed through a nitric acid wet etch. The VCPAs are formed by depositing a 5 nm titanium adhesion layer and a 35 nm plasmon active gold layer onto the nanopillar template. Gold has inferior SERS enhancement factors compared to silver, but is stable under ambient conditions and does not suffers from oxidation[97]. The plasmonic slab consists of a perforated gold film at the base of the pillars and a dot array on top of the pillars. The gold dots on top of the nanopillars extend slightly over the silicon nanopillar base and have an average diameter of d = 33.7 nm ± 7.1 nm (Figure 5.2D and diameter histogram in figure S8). This is advantageous since it increases the surface area at the main hot-spot locations. Furthermore, the small standard deviation of the gold dot diameter reduces inhomogeneous broadening of the plasmon resonance that can lower the SERS intensity[125]. Concluding, a series of angled views of the VCPAs with different heights is shown in figure 5.3 and S8.

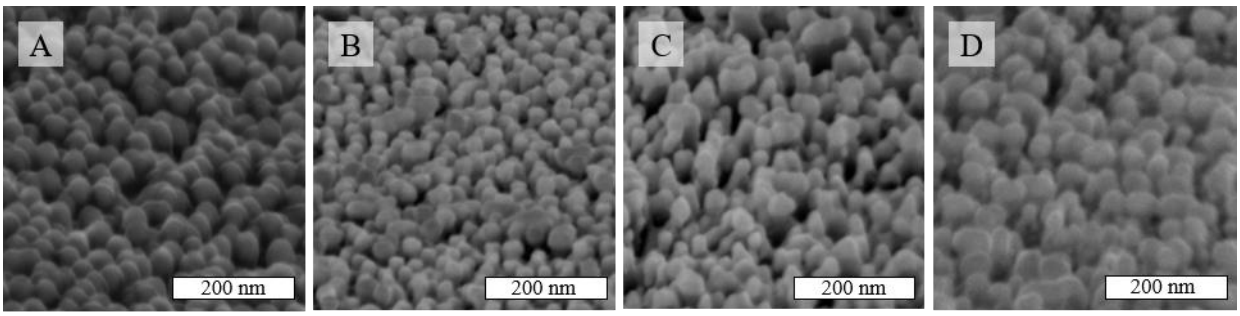

Figure 5.3 SEM images of VCPAS with different heights at a 70° angle. (A) 55 nm (B) 65 nm (C) 74 nm (D) 91 nm.

5.2 SERS measurements

4-ATP was selected as a probe molecule as the thiol group can form covalently strong bonds with the gold surface. Moreover, the molecule was already used as a SERS probe and the vibrational bands at the finger print region were assigned [126]. A special feature of 4-ATP molecules is its capability to oxidize to 4,4'-dimercaptoazobenzene (DMAB) during SERS experiments[127]. The VCPAs were immersed into 1 mM 4-aminothiophenol (4-ATP) for 12 hours to self-assemble a single monolayer onto the gold surface and was then thoroughly rinsed with milli-Q water to remove any excess molecules. In the study only the C-S bond stretching vibration coupled to the $7a(a_1)_3$ benzene ring stretching vibration mode at the ~1075 cm^{-1} peak was considered as it has similar SERS line shapes and intensities for both molecules[127]. In figure 5.4(A) the normalized SERS spectra and normal Raman of bulk 4-ATP is shown (look in the appendix for detailed methodology). Strongest peak is the C-S, $7a(a_1)_3$ str vibration at ~1075 cm^{-1} . The SERS spectra shows its typical broad continuum background and the line shapes of the molecules are broadened compared to the bulk 4-ATP Raman spectra[128]. The latter is especially useful when using a low resolution Raman spectrometer. To demonstrate that our block-copolymer-derived templates are a reliable platform for SERS a 200 µm × 200 µm map of the background-corrected

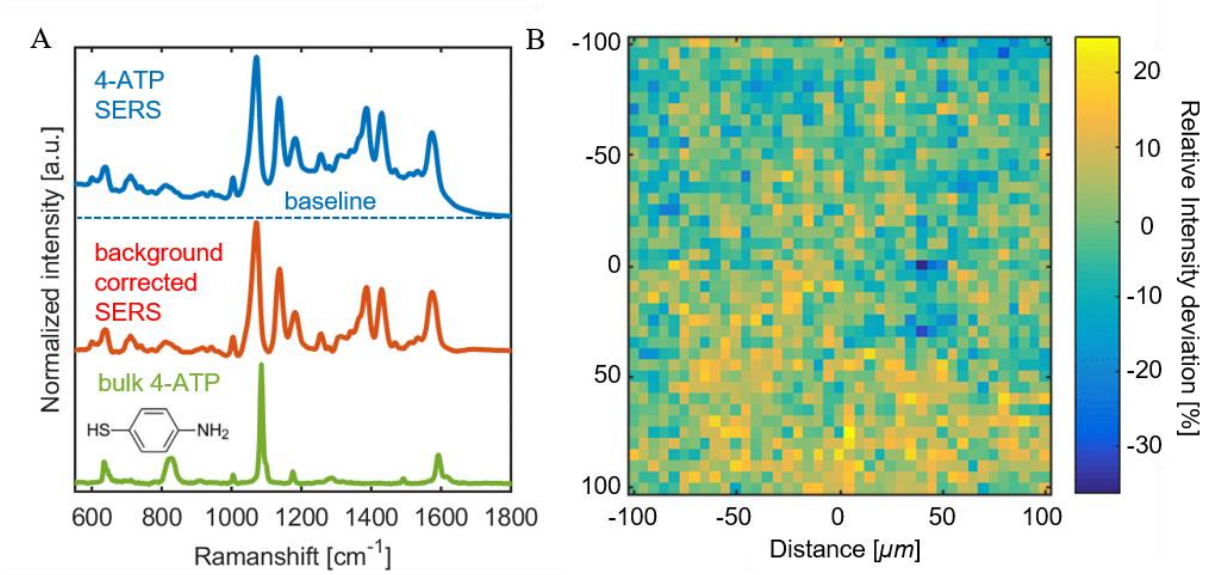

Figure 5.4 (A) SERS, background corrected SERS and Raman spectra of 4-ATP. The spectra were normalized to their maximum Raman scattering intensity for better visual comparison. (B) 200 µm × 200 µm map of the background corrected Raman intensity deviation to its mean value. The C-S, 7(a_1)$_3$ stretch vibration peak at 1075 cm^{-1} and a 5x objective (NA = 0.25) with 4 µm laser diameter was used with a 5 µm mapping resolution.

SERS intensity was measured. It showed an average relative standard deviation of 8% (figure 5.4(B)). Further, the effect of the nanopillar height on the SERS enhancement factor was investigated (figure 5.5). It is assumed that the gold surface of the VCPAs are fully covered by 4-ATP molecules and all the molecules contribute to the Raman signal. The SERS enhancement drastically increases for shorter pillar heights and smaller inter slab gaps, which exhibits stronger coupling between the disk array and the perforated gold film at the base of the pillars.. Generally, the electric near field enhancement increases exponentially with decreasing plasmonic gap size[129]. However, it will also shift the plasmon resonance position and a careful optimization must be done to adjust the plasmon resonance to the laser wavelength. However, smaller plasmonic gaps will generally enhance the Raman intensity and therefore smaller pillar heights should perform better[130]. The strongest experimental enhancement factor is calculated

to be 1×10^7 for nanopillars with h = 55 nm and a gap between the metal films below 15 nm. The size of the plasmonic gaps is large enough to allow a functionalisation of the gold surface and leave enough space to be accessible for larger macromolecules such as proteins[131]. This is an average SERS enhancement factor assuming that all the molecules contribute equally to the SERS intensity. If one make an unlikely assumption like in Ref[118] that only the molecules in the plasmonic hot spots contribute the Raman signal, then the SERS enhancement factor can be several magnitudes higher[16]. To put this into perspective Ru et. al demonstrated that EFs as low as 10^7 are sufficient for single molecule SERS signals whereas typical maximum single molecule SERS experiments are performed with enhancement factors at the order of ~10^{10} [132]. Hence, it can be anticipated that the VCPAs should be capable of single molecule spectroscopy.

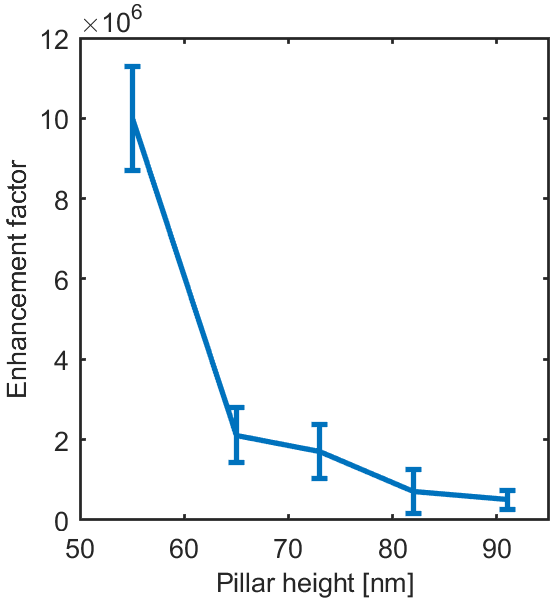

Figure 5.5 Experimental enhancement factor of VCPAs with different pillar heights. The metal thickness coated on the nanopillar array template is 40 nm.

5.3 FDTD simulation

To investigate the origin of the large enhancement factor finite difference time domain (FDTD) simulations were performed to predict the electromagnetic hot spots. In the simplest approximation the SERS enhancement scales with the 4th power of the electric field enhancement $I_{SERS} \propto < E^4/E_0^4 >$ where E is the electric field at the surface of the plasmonic structure which is normalized to the electric field of the incident light E_0. First, only the nanopillars without any gold were simulated. Figure 5.6(A) shows the cross section of the electric field enhancement. As expected, the near field enhancement is negligible without plasmon resonance. Further, the cross section of the nanopillars can be seen with only dots on top of the nanopillars (Figure 5.6(B)), a perforated gold film at the base of the nanopillars (Figure 5.6(C)) and VCPAs (Figure 5.6(D)) at plasmon resonance. Clearly, there is a strong near field enhancement in between the vertical gap of the plasmonic slabs. In figure 5.6(E) the near field enhancement as a function of wavelength is shown. The VCPAs do not only feature larger electric field enhancements than the respective individual hole array and disk array, but the plasmon resonance and the near field enhancement is also broader.

The strong enhancement of the VCPAs is attributed to Babinet's principle[6]. Babinet's principle states that the transmittance (T) of a slab and its complementary counterpart (T_C) should fulfil $T+T_C=1$. This indicates that the resonance position of the hole array and that of the disk array should be somewhat similar. Therefore the plasmonic resonance can be seen analogue to the coupling of nanoparticle dimers[91]. Accordingly, the plasmon coupling can be tuned by the gap size between hole array and disk array[6] and therefore also the electric field enhancement.

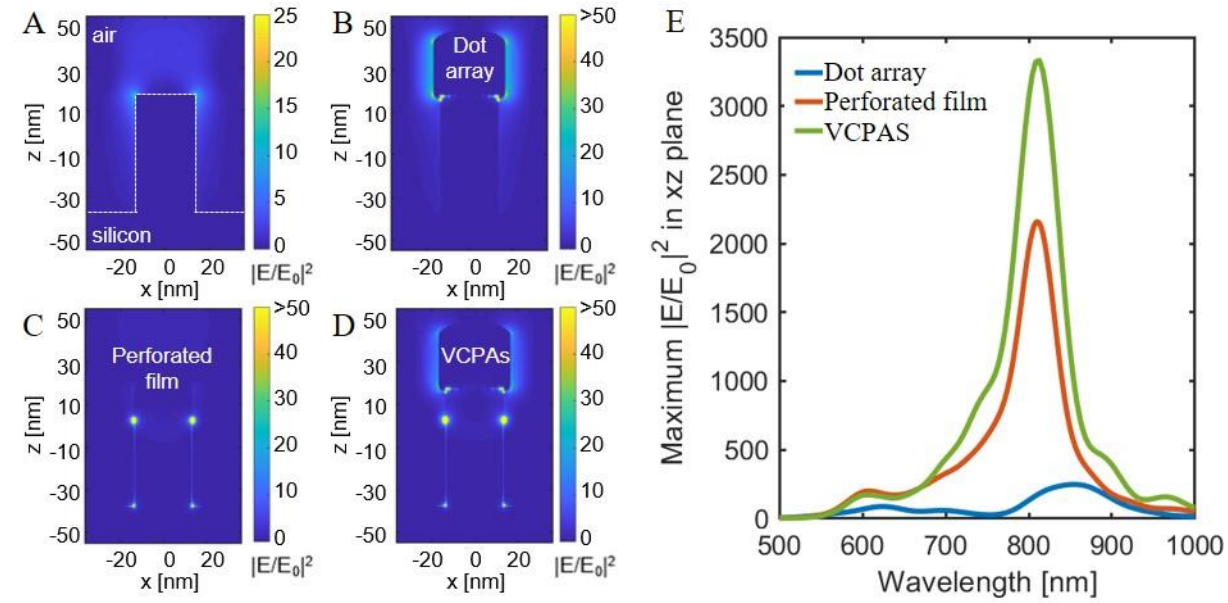

Figure 5.6 Cross section of the simulated electric field enhancement (A-D). (A) Silicon nanopillar with 55 nm height. (B) Gold dot array on top of the nanopillars, (C) Nanopillars perforating a thin gold film at plasmon resonance and (D) VCPAs at plasmon resonance. (E) Electric field enhancement as a function of wavelength for dot arrays, perforated gold film and VCPAs. The VCPAs perform equal or better than the respective perforated film and dot array for any wavelength.

5.4 Discussion and outlook

The VCPAs demonstrate an excellent average enhancement factors as high as 1×10^7 with a standard deviation of the Raman intensity up to 8%. To put this into perspective let us consider the most important commercial available SERS substrates. (I) Klarite (Mesophotonics Ltd., Southampton, UK) is based on photolithography and potassium hydroxide (KOH) wet etching . of silicon to create inverted pyramids that are then coated with gold. In addition, the silicon monolith can be used for injection moulding to create plastic SERSs substrates. The enhancement is reported to be between 10^2 and 10^9 with a standard deviation of 5%[133, 134]. Due to the fact that the inverted pyramids do not feature sharp edges or nanogaps it is reasonable to assume that the true enhancement factor is at the lower end of reported values (wrong or elevated enhancement factors are quiete common in literature[132]). (II) Serstrates (Silmeco, Copenhagen,

DK) are based on maskless reactive ion etching and have enhancement factor as high as 6.24 × 10^6 with a standard deviation of 7%[16]. The block copolymer derived SERS templates have a superior enhancement factor,f but the standard deviation is slightly lower than the commercial available substrates. However, the sample fabrication in cleanroom facilities should improve the overall quality of the substrates. The process fabrication can also be further optimised. Due to the small required aspect ratios of the VCPAs a polymer soft mask can be used instead of a metal oxide hard mask. Poly(styrene)-*b*-poly(methyl methacrylate) (PS-*b*-PMMA) is suitable for pattern transfer. The PMMA can be degraded in UV/ozone or oxygenated plasma and then removed, whereas the PS gets cross linked and can be used as a mask[135]. Next, the pillars can be created with KOH on <110> orientated silicon for an almost perpendicular etch (instead of inverse pyramidal for <100> orientation)[136]. Finally, gold can be wet chemically deposited onto the template [137]. Gold evaporation is a lengthy process that involves costly equipment. In contrast, a wet chemical preparation is cheaper , requires little equipment and can be also performed by the end-user if the template is to be recycled[110].

The VCPAs feature an unique option for spectro-electrochemistry. The perforated gold film at the base of the pillars can be used as an electrode. Soluble proteins and other biomolecules have in general surface charges to mediate interaction with polar solvent (water). A potential at the electrode could attract these molecules directly into the plasmonic hot spots (Figure. 5.7(A)). As an example such a set up could be used for the rapid analysis of antigens in blood, milk or urine[113, 138]. The pillars itself can be also used to filter larger macro molecules and to reduce noise in the Raman signal. This concept is already used on microstructured ATR crystals provided by Irubis (Munich, Germany).

The VCPAs are also very interesting for molecular biophysics. It is often desirable to have a free standing lipid bilayer membranes for protein studies[139]. Membranes that are supported on a substrate do prevent the transmembrane proteins from interacting with the substrate, which denatures proteins[139]. A membrane spanning on top of the VCPAs could support functional proteins in the membrane section between the pillars. Considering that the vibrational enhancement is strong enough, the pump activity of channel proteins can be monitored by SERS, where the perforated film can act as an electrode. In the case of voltage-gated ion channels the closing and opening of the channel can then be controlled by the potential of the electrode (Figure 5.7(B)).

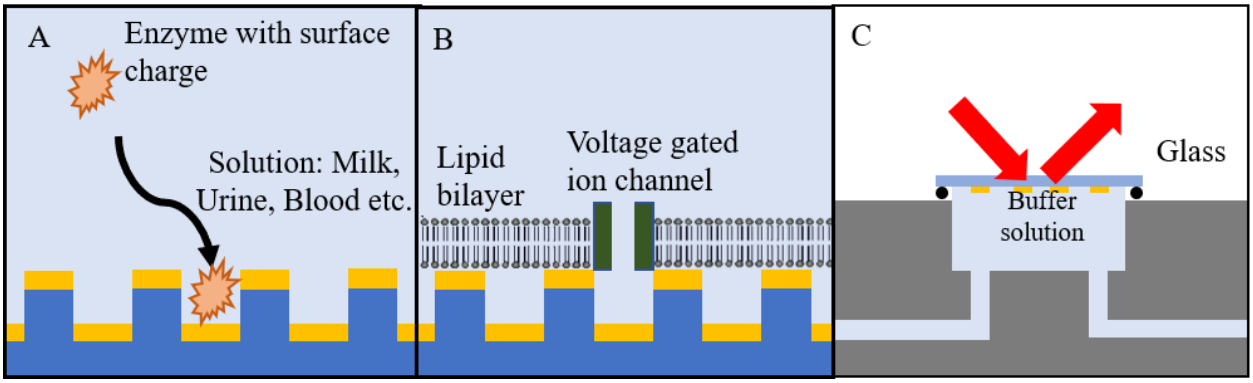

Figure 5.7 Potential application of the VCPA SERS sensor. (A) The perforated at the base of the pillars can be used an electrode to attract charged molecules. (B) The electrode can be also used to monitor the activity of voltage-gated ion channels for spectro-electrochemistry. (C) Internal reflection configuration with transparent substrate such as glass/fused silica in combination with microfluidic cell.

The silicon substrate and silicon nanopillars are also highly polarizable due to the large refractive index that results in a slight electric screening. A different material with a smaller refractive index such as SiO_2 could reduce it, however this will change the plasmonic resonance position and an optimisation of the geometrical parameters is necessary. In addition, glass/fused silica is

transparent which allows for internal reflection configurations. This is useful when measuring in fluidic medium where otherwise a costly water immersion objective is required. For example glass as a substrate can be used in a microfluidic setup [140] such as depicted in figure 5.7(C) or for total internal reflection fluorescence microscopy [15].

6. Acknowledgement

This work was partially funding by the European Union's Horizon 2020 research and innovation program under grant agreement No 760915 (SUN-PILOT). I gratefully thank Parvaneh Mokarian-Tabari and members of INSG for their full support within their best scope of capabilities and Prof. Reich (Freie Universität Berlin) and Prof. Morris for full access to their labs and equipment. I gratefully acknowledge the Advanced Microscopy Laboratory (AML), Trinity College Dublin for access to their SEM facilities. Calculations were partially performed on the Kelvin cluster maintained by the Trinity Centre for High Performance Computing. This cluster was funded through grants from the Higher Education Authority of Ireland, through its PRTLI program. I also like to thank Brian Jennings, Neal O'Hara, Sören Waßerroth, Ömer Akay. Georgy Gordev, Sajjad Husain Mir, Elsa Giraud, Gaulthier Rydzek, Riley Gatensby and my brother Eser Metin Akinoglu for fruitful discussion or technical support.

7. Appendix

7.1 Raman spectroscopy

SERS spectra were collected with a XploRA Raman spectrometer equipped with a 785 nm wavelength laser. The power was set to 0.54 mW. A 100x objective (NA=0.9) was used with a beam focus width of 1 µm. The integration time were 5 seconds with 5 accumulations for each spectrum. 10 spectra from different spots were averaged and the baseline were corrected from their characteristic background. The enhancement factor was estimated with following expression:

$$EF = \frac{I_{SERS}/N_{SERS}}{I_{REF}/N_{REF}}$$

where I_{SERS} and I_{REF} are the Raman intensities and N_{SERS} and N_{REF} are the probed molecules for the SERS and reference measurement respectively. For N_{SERS} all the molecules self-assembled on the gold surface of the VCPAs are counted with a surface packing density of 0.20 nm^2 per molecule[141]. The effective VCPAs surface is estimated to be two times larger than the corresponding flat surface, which leads to an estimate of 7.85×10^6 molecules probes. N_{REF} is calculated by collecting a spectra of bulk 4-ATP with a molecular density of 1.18 g/cm^3. Assuming a laser interaction volume of ~ 15 μm^3 and a molecular weight of 125.189 g/mol, we calculated N_{REF} to be 8.8×10^{10}. The laser interaction volume and height were determined as discussed in Ref. [132].The calculated enhancement factor can be seen as an upper limit. The mapping in figure 2B was collected with 785 nm wavelength and 5x objective with 4 μm laser diameter and 5 μm resolution. Two 200 $\mu m \times 100$ μm (the full range of our Piezo stage) were collected next to each other and subsequently merged for further analysis.

7.2 Supplemental figures

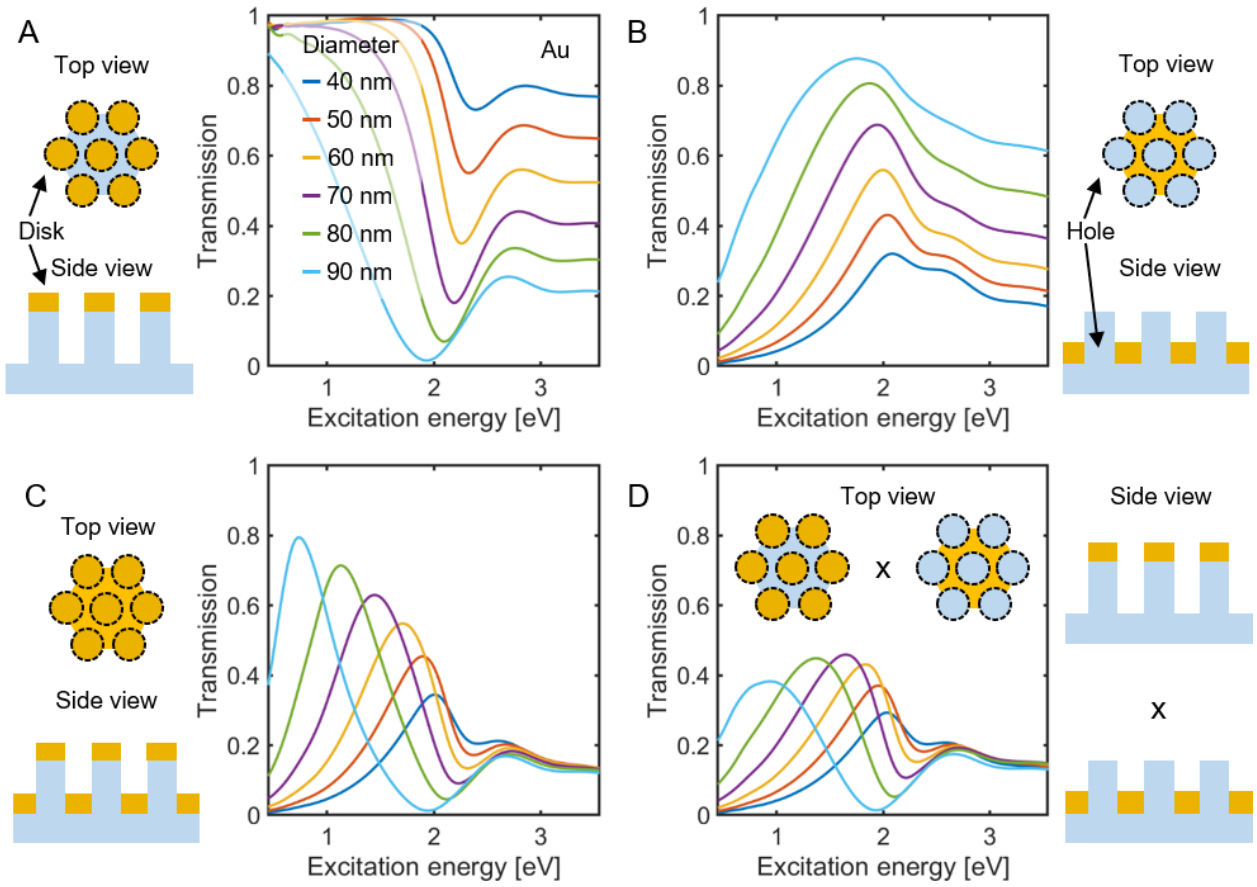

Figure S1. Respective figures in Fig 4.1 in eV instead of wavelength.

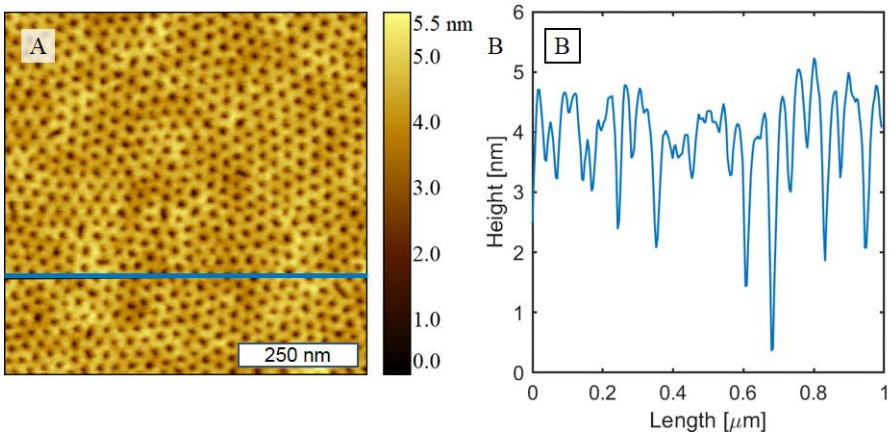

Figure S2. PS-b-PEO after phase separation. (A) AFM picture. (B) AFM profile line.

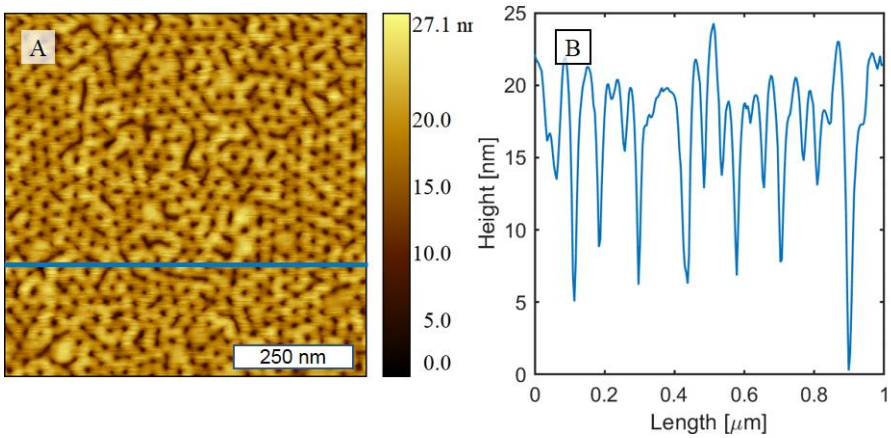

Figure S3. PS-b-PEO after swelling. (A) AFM picture. (B) AFM profile line.

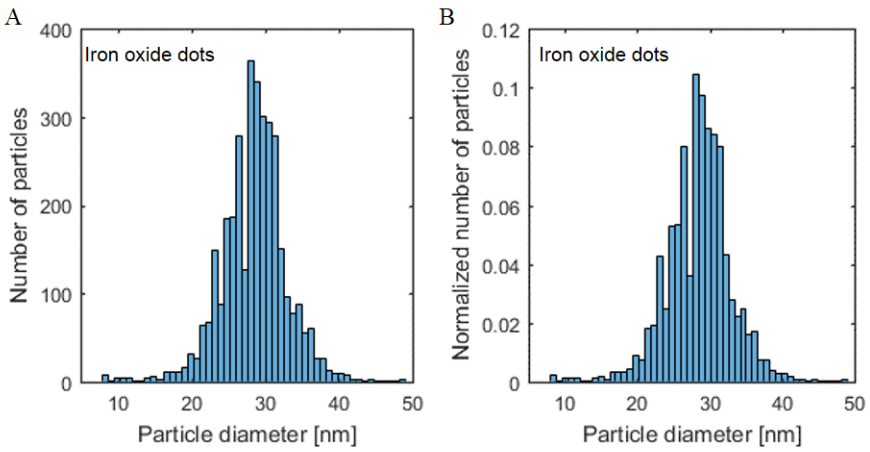

Figure S4. Particle size distribution of the iron oxide particles: (A) absolute and (B) relative.

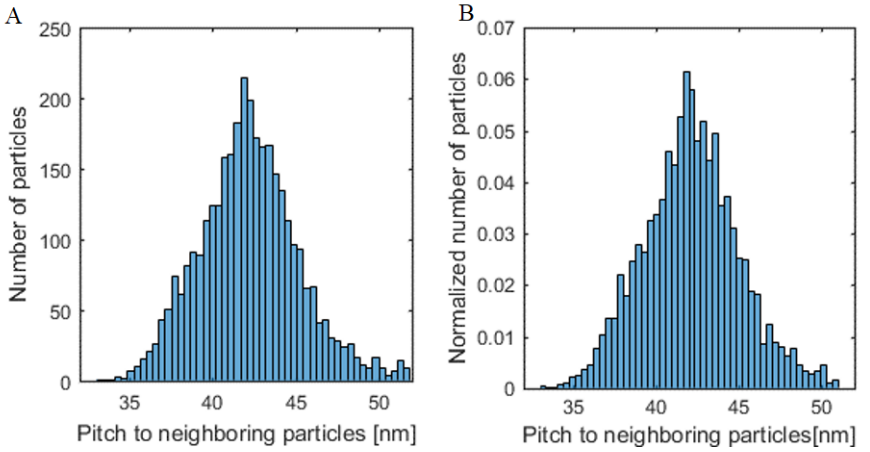

Figure S5. Iron oxide nanoparticle pitch: (A) absolute and (B) relative.

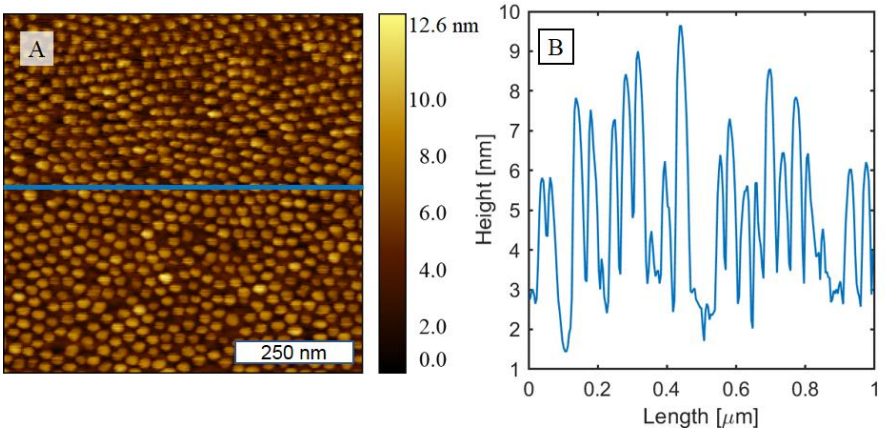

Figure S6. Iron oxide hard mask (A) AFM picture. (B) AFM profile line.

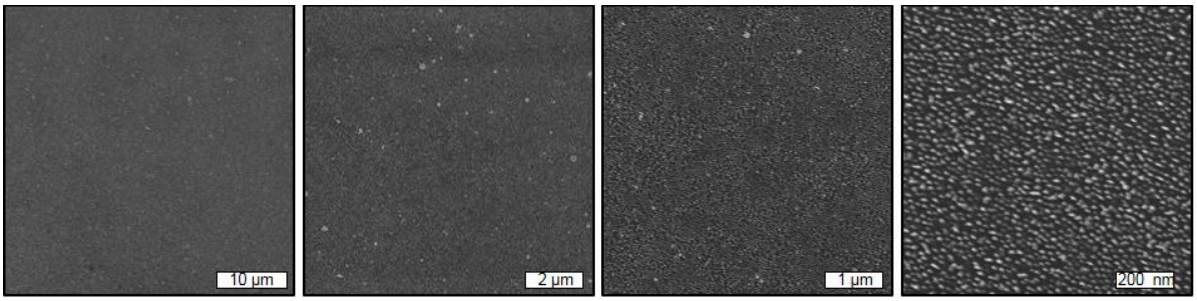

Figure S7. SEM top view with different magnifications of nanopillars before iron oxide removal

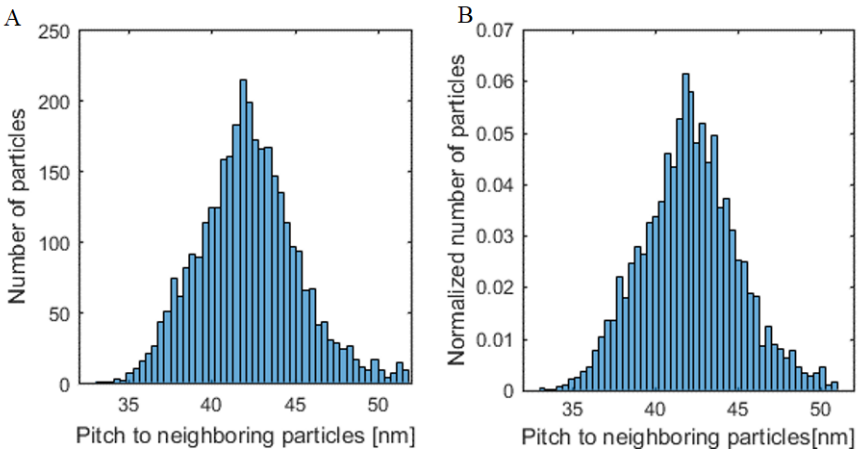

Figure S8. Particle size distribution of the gold dots on top of the nanopillars: (A) absolute and (B) relative.

8. References

1. Gu, Y.; Zhang, L.; Yang, J. K. W.; Yeo, S. P.; Qiu, C.-W., Color generation via subwavelength plasmonic nanostructures. *Nanoscale* **2015,** *7* (15), 6409-6419.

2. Williams, C.; Rughoobur, G.; Flewitt, A. J.; Wilkinson, T. D., Nanostructured plasmonic metapixels. *Scientific Reports* **2017,** *7* (1), 7745.

3. Mudachathi, R.; Tanaka, T., Up Scalable Full Colour Plasmonic Pixels with Controllable Hue, Brightness and Saturation. *Scientific Reports* **2017,** *7* (1), 1199.

4. Kumar, K.; Duan, H.; Hegde, R. S.; Koh, S. C. W.; Wei, J. N.; Yang, J. K. W., Printing colour at the optical diffraction limit. *Nature Nanotechnology* **2012,** *7*, 557.

5. Ellenbogen, T.; Seo, K.; Crozier, K. B., Chromatic Plasmonic Polarizers for Active Visible Color Filtering and Polarimetry. *Nano Letters* **2012,** *12* (2), 1026-1031.

6. Akinoglu, G. E.; Akinoglu, E. M.; Kempa, K.; Giersig, M., Plasmon resonances in coupled Babinet complementary arrays in the mid-infrared range. *Optics Express* **2019,** *27* (16), 22939-22950.

7. Lal, S.; Clare, S. E.; Halas, N. J., Nanoshell-Enabled Photothermal Cancer Therapy: Impending Clinical Impact. *Accounts of Chemical Research* **2008,** *41* (12), 1842-1851.

8. Tang, L.; Li, J., Plasmon-Based Colorimetric Nanosensors for Ultrasensitive Molecular Diagnostics. *ACS Sensors* **2017,** *2* (7), 857-875.

9. Hou, W.; Cronin, S. B., A review of surface plasmon resonance-enhanced photocatalysis. *Advanced Functional Materials* **2013,** *23* (13), 1612-1619.

10. Caldwell, J. D.; Glembocki, O.; Bezares, F. J.; Bassim, N. D.; Rendell, R. W.; Feygelson, M.; Ukaegbu, M.; Kasica, R.; Shirey, L.; Hosten, C., Plasmonic nanopillar arrays for large-area, high-enhancement surface-enhanced Raman scattering sensors. *ACS nano* **2011,** *5* (5), 4046-4055.

11. Tabatabaei, M.; Najiminaini, M.; Davieau, K.; Kaminska, B.; Singh, M. R.; Carson, J. J. L.; Lagugné-Labarthet, F., Tunable 3D Plasmonic Cavity Nanosensors for Surface-Enhanced Raman Spectroscopy with Sub-femtomolar Limit of Detection. *ACS Photonics* **2015,** *2* (6), 752-759.

12. Li, W.-D.; Ding, F.; Hu, J.; Chou, S. Y., Three-dimensional cavity nanoantenna coupled plasmonic nanodots for ultrahigh and uniform surface-enhanced Raman scattering over large area. *Optics express* **2011,** *19* (5), 3925-3936.

13. Chen, X.; Wang, C.; Yao, Y.; Wang, C., Plasmonic Vertically Coupled Complementary Antennas for Dual-Mode Infrared Molecule Sensing. *ACS Nano* **2017,** *11* (8), 8034-8046.

14. Weihua, Z.; Fei, D.; Wen-Di, L.; Yuxuan, W.; Jonathan, H.; Stephen, Y. C., Giant and uniform fluorescence enhancement over large areas using plasmonic nanodots in 3D resonant cavity nanoantenna by nanoimprinting. *Nanotechnology* **2012,** *23* (22), 225301.

15. Block, S.; Aćimović, S. S.; Odebo Länk, N.; Käll, M.; Höök, F., Antenna-Enhanced Fluorescence Correlation Spectroscopy Resolves Calcium-Mediated Lipid–Lipid Interactions. *ACS Nano* **2018,** *12* (4), 3272-3279.

16. Schmidt, M. S.; Hübner, J.; Boisen, A., Large area fabrication of leaning silicon nanopillars for surface enhanced Raman spectroscopy. *Advanced Materials* **2012,** *24* (10), OP11-OP18.

17. Bezares, F. J.; Caldwell, J. D.; Glembocki, O.; Rendell, R. W.; Feygelson, M.; Ukaegbu, M.; Kasica, R.; Shirey, L.; Bassim, N. D.; Hosten, C., The Role of Propagating and Localized Surface Plasmons for SERS Enhancement in Periodic Nanostructures. *Plasmonics* **2012,** *7* (1), 143-150.

18. Langer, J.; Jimenez de Aberasturi, D.; Aizpurua, J.; Alvarez-Puebla, R. A.; Auguié, B.; Baumberg, J. J.; Bazan, G. C.; Bell, S. E. J.; Boisen, A.; Brolo, A. G.; Choo, J.; Cialla-May, D.; Deckert, V.; Fabris, L.; Faulds, K.; García de Abajo, F. J.; Goodacre, R.; Graham, D.; Haes, A. J.; Haynes, C. L.; Huck, C.; Itoh, T.; Käll, M.; Kneipp, J.; Kotov, N. A.; Kuang, H.; Le Ru, E. C.; Lee, H. K.; Li, J.-F.; Ling, X. Y.; Maier, S.; Mayerhoefer, T.; Moskovits, M.; Murakoshi, K.; Nam, J.-M.; Nie, S.; Ozaki, Y.; Pastoriza-Santos, I.; Perez-Juste, J.; Popp, J.; Pucci, A.; Reich, S.; Ren, B.; Schatz, G. C.; Shegai, T.; Schlücker, S.; Li-Lin, T.; Thomas, K. G.; Tian, Z.-Q.; Van Duyne, R. P.; Vo-Dinh, T.; Wang, Y.; Willets, K. A.; Xu, C.; Xu, H.; Xu, Y.; Yamamoto, Y. S.; Zhao, B.; Liz-Marzán, L. M., Present and Future of Surface Enhanced Raman Scattering. *ACS Nano* **2019,** *14* (1), 28-117.

19. Bates, C. M.; Maher, M. J.; Janes, D. W.; Ellison, C. J.; Willson, C. G., Block Copolymer Lithography. *Macromolecules* **2014,** *47* (1), 2-12.

20. Cummins, C.; Ghoshal, T.; Holmes, J. D.; Morris, M. A., Strategies for inorganic incorporation using neat block copolymer thin films for etch mask function and nanotechnological application. *Advanced Materials* **2016,** *28* (27), 5586-5618.

21. Mokarian-Tabari, P.; Senthamaraikannan, R.; Glynn, C.; Collins, T. W.; Cummins, C.; Nugent, D.; O'Dwyer, C.; Morris, M. A., Large block copolymer self-assembly for fabrication of subwavelength nanostructures for applications in optics. *Nano letters* **2017,** *17* (5), 2973-2978.

22. Möller, M.; Spatz, J. P.; Roescher, A.; Mößmer, S.; Selvan, S. T.; Klok, H.-A., Mineralization of gold in block copolymer micelles. *Macromolecular Symposia* **1997,** *117* (1), 207-218.

23. Ghoshal, T.; Cruz-Romero, M. C.; Kerry, J. P.; Morris, M. A., Nanosize and Shape Effects on Antimicrobial Activity of Silver Using Morphology-Controlled Nanopatterns by Block Copolymer Fabrication. *ACS Applied Nano Materials* **2019,** *2* (10), 6325-6333.

24. Cheng, C.-F.; Hsueh, H.-Y.; Lai, C.-H.; Pan, C.-J.; Hwang, B.-J.; Hu, C.-C.; Ho, R.-M., Nanoporous gyroid platinum with high catalytic activity from block copolymer templates via electroless plating. *NPG Asia Materials* **2015,** *7* (4), e170.

25. Kimling, J.; Maier, M.; Okenve, B.; Kotaidis, V.; Ballot, H.; Plech, A., Turkevich method for gold nanoparticle synthesis revisited. *The Journal of Physical Chemistry B* **2006,** *110* (32), 15700-15707.

26. Maier, S. A., Plasmonics: fundamentals and applications. Springer Science & Business Media: 2007.

27. Stuart, M. A. C.; Huck, W. T. S.; Genzer, J.; Müller, M.; Ober, C.; Stamm, M.; Sukhorukov, G. B.; Szleifer, I.; Tsukruk, V. V.; Urban, M.; Winnik, F.; Zauscher, S.; Luzinov, I.; Minko, S., Emerging applications of stimuli-responsive polymer materials. *Nature Materials* **2010,** *9* (2), 101-113.

28. Wei, M.; Gao, Y.; Li, X.; Serpe, M. J., Stimuli-responsive polymers and their applications. *Polymer Chemistry* **2017,** *8* (1), 127-143.

29. Kim, J. Y.; Kim, H.; Kim, B. H.; Chang, T.; Lim, J.; Jin, H. M.; Mun, J. H.; Choi, Y. J.; Chung, K.; Shin, J.; Fan, S.; Kim, S. O., Highly tunable refractive index visible-light metasurface from block copolymer self-assembly. *Nature Communications* **2016,** *7* (1), 12911.

30. Gérard, D.; Gray, S. K., Aluminium plasmonics. *Journal of Physics D: Applied Physics* **2014,** *48* (18), 184001.

31. Telecka, A.; Li, T.; Ndoni, S.; Taboryski, R., Nanotextured Si surfaces derived from block-copolymer self-assembly with superhydrophobic, superhydrophilic, or superamphiphobic properties. *RSC Advances* **2018,** *8* (8), 4204-4213.

32. Tseng, M. L.; Yang, J.; Semmlinger, M.; Zhang, C.; Nordlander, P.; Halas, N. J., Two-Dimensional Active Tuning of an Aluminum Plasmonic Array for Full-Spectrum Response. *Nano Letters* **2017,** *17* (10), 6034-6039.

33. Ghorbani, H. R., A review of methods for synthesis of Al nanoparticles. *Oriental Journal of Chemistry* **2014,** *30* (4), 1941-1949.

34. Yi, D. H.; Nam, C.-Y.; Doerk, G.; Black, C. T.; Grubbs, R. B., Infiltration Synthesis of Diverse Metal Oxide Nanostructures from Epoxidized Diene–Styrene Block Copolymer Templates. *ACS Applied Polymer Materials* **2019,** *1* (4), 672-683.

35. Kästle, G.; Boyen, H. G.; Weigl, F.; Lengl, G.; Herzog, T.; Ziemann, P.; Riethmüller, S.; Mayer, O.; Hartmann, C.; Spatz, J. P.; Möller, M.; Ozawa, M.; Banhart, F.; Garnier, M. G.; Oelhafen, P., Micellar Nanoreactors—Preparation and Characterization of Hexagonally Ordered Arrays of Metallic Nanodots. *Advanced Functional Materials* **2003,** *13* (11), 853-861.

36. Lohmüller, T.; Aydin, D.; Schwieder, M.; Morhard, C.; Louban, I.; Pacholski, C.; Spatz, J. P., Nanopatterning by block copolymer micelle nanolithography and bioinspired applications. *Biointerphases* **2011,** *6* (1), MR1-MR12.

37. Mir, S. H.; Rydzek, G.; Nagahara, L. A.; Khosla, A.; Mokarian-Tabari, P., Review—Recent Advances in Block-Copolymer Nanostructured Subwavelength Antireflective Surfaces. *Journal of The Electrochemical Society* **2019,** *167* (3), 037502.

38. Tolenis, T.; Grinevičiūtė, L.; Buzelis, R.; Smalakys, L.; Pupka, E.; Melnikas, S.; Selskis, A.; Drazdys, R.; Melninkaitis, A., Sculptured anti-reflection coatings for high power lasers. *Optical Materials Express* **2017,** *7* (4), 1249-1258.

39. Raut, H. K.; Ganesh, V. A.; Nair, A. S.; Ramakrishna, S., Anti-reflective coatings: A critical, in-depth review. *Energy & Environmental Science* **2011,** *4* (10), 3779-3804.

40. Kozuch, D. J.; Zhang, W.; Milner, S. T., Predicting the Flory-Huggins χ Parameter for Polymers with Stiffness Mismatch from Molecular Dynamics Simulations. **2016,** *8* (6), 241.

41. Bates, F. S.; Fredrickson, G. H., Block Copolymer Thermodynamics: Theory and Experiment. **1990,** *41* (1), 525-557.

42. Sinturel, C.; Vayer, M.; Morris, M.; Hillmyer, M. A., Solvent Vapor Annealing of Block Polymer Thin Films. *Macromolecules* **2013,** *46* (14), 5399-5415.

43. Mokarian-Tabari, P.; Collins, T. W.; Holmes, J. D.; Morris, M. A., Cyclical "Flipping" of Morphology in Block Copolymer Thin Films. *ACS Nano* **2011,** *5* (6), 4617-4623.

44. Ghoshal, T.; Senthamaraikannan, R.; Shaw, M.; Holmes, J.; Morris, M., In situ hard mask materials: A new methodology for creation of vertical silicon nanopillar and nanowire arrays. *Nanoscale* **2012,** *4*.

45. Giraud, E. C.; Mokarian-Tabari, P.; Toolan, D. T.; Arnold, T.; Smith, A. J.; Howse, J. R.; Topham, P. D.; Morris, M. A., Highly Ordered Titanium Dioxide Nanostructures via a Simple One-Step Vapor-Inclusion Method in Block Copolymer Films. *ACS Applied Nano Materials* **2018,** *1* (7), 3426-3434.

46. Ghoshal, T.; O'Connell, J.; Sinturel, C.; Andreazza, P.; Holmes, J. D.; Morris, M. A., Solvent mediated inclusion of metal oxide into block copolymer nanopatterns: Mechanism of oxide formation under UV-Ozone treatment. *Polymer* **2019,** *173*, 197-204.

47. Zou, H., Anisotropic Si deep beam etching with profile control using SF6/O2 Plasma. *Microsystem Technologies* **2004,** *10* (8), 603-607.

48. Dialameh, M.; Lupi, F. F.; Imbraguglio, D.; Zanenga, F.; Lamperti, A.; Martella, D.; Seguini, G.; Perego, M.; Rossi, A.; De Leo, N., Influence of block copolymer feature size on reactive ion etching pattern transfer into silicon. *Nanotechnology* **2017,** *28* (40), 404001.

49. d'Agostino, R.; Flamm, D. L., Plasma etching of Si and SiO2 in SF6–O2 mixtures. *Journal of Applied Physics* **1981,** *52* (1), 162-167.

50. Wang, Y.; Plummer, E. W.; Kempa, K., Foundations of Plasmonics. *Advances in Physics* **2011,** *60* (5), 799-898.

51. Drude, P., Zur Elektronentheorie der Metalle. *Annalen der Physik* **1900,** *306* (3), 566-613.

52. Bochterle, J. Nanoantennenverstärkte Infrarotspektroskopie von Molekülen. Dissertation, Universität Heidelberg, Universität Heidelberg, 2013.

53. Willets, K. A.; Duyne, R. P. V., Localized Surface Plasmon Resonance Spectroscopy and Sensing. *Annual Review of Physical Chemistry* **2007,** *58* (1), 267-297.

54. Pitarke, J. M.; Silkin, V. M.; Chulkov, E. V.; Echenique, P. M., Theory of surface plasmons and surface-plasmon polaritons. *Reports on Progress in Physics* **2007,** *70* (1), 1.

55. Raether, H., *Surface plasmons on smooth and rough surfaces and on gratings*. Springer: 1988.

56. Anatoly, V. Z.; Igor, I. S., Near-field photonics: surface plasmon polaritons and localized surface plasmons. *Journal of Optics A: Pure and Applied Optics* **2003,** *5* (4), S16.

57. Lu, X.; Rycenga, M.; Skrabalak, S. E.; Wiley, B.; Xia, Y., Chemical Synthesis of Novel Plasmonic Nanoparticles. *Annual Review of Physical Chemistry* **2009,** *60* (1), 167-192.

58. Jackson, J. D., *Classical Electrodynamics*. Wiley: 2007.

59. Osawa, M.; Ikeda, M., Surface-enhanced infrared absorption of p-nitrobenzoic acid deposited on silver island films: contributions of electromagnetic and chemical mechanisms. *The Journal of Physical Chemistry* **1991,** *95* (24), 9914-9919.

60. Zentgraf, T.; Meyrath, T. P.; Seidel, A.; Kaiser, S.; Giessen, H.; Rockstuhl, C.; Lederer, F., Babinet's principle for optical frequency metamaterials and nanoantennas. *Physical Review B* **2007,** *76* (3), 033407.

61. Huck, C.; Vogt, J.; Sendner, M.; Hengstler, D.; Neubrech, F.; Pucci, A., Plasmonic Enhancement of Infrared Vibrational Signals: Nanoslits versus Nanorods. *ACS Photonics* **2015,** *2* (10), 1489-1497.

62. Falcone, F.; Lopetegi, T.; Laso, M. A. G.; Baena, J. D.; Bonache, J.; Beruete, M.; Marqués, R.; Martín, F.; Sorolla, M., Babinet Principle Applied to the Design of Metasurfaces and Metamaterials. *Physical Review Letters* **2004,** *93* (19), 197401.

63. Taflove, A.; Hagness, S. C., Computational Electrodynamics, The Finite-Difference Time-Domain Method. Norwood: Artech House: 2000.

64. Yee, K. S., Numerical Solution of Initial Boundary Value Problems Involving Maxwell's Equations in Isotropic MEdia. *Antennas Propagation* **1966,** *14*, 302.

65. Oskooi, A. F.; Roundy, D.; Ibanescu, M.; Bermel, P.; Joannopoulos, J. D.; Johnson, S. G., MEEP: A flexible free-software package for electromagnetic simulations by the FDTD method. *Computer Physics Communications* **2010,** *181* (3), 687-702.

66. Oskooi, A. F.; Zhang, L.; Avniel, Y.; Johnson, S. G., The failure of perfectly matched layers, and towards their redemption by adiabatic absorbers. *Optics Express* **2008,** *16* (15), 11376-11392.

67. Rakić, A. D.; Djurišić, A. B.; Elazar, J. M.; Majewski, M. L., Optical properties of metallic films for vertical-cavity optoelectronic devices. *Appl. Opt.* **1998,** *37* (22), 5271-5283.

68. Li, W.; Jiang, X.; Xue, J.; Zhou, Z.; Zhou, J., Antibody modified gold nano-mushroom arrays for rapid detection of alpha-fetoprotein. *Biosensors and Bioelectronics* **2015,** *68*, 468-474.

69. Shen, Y.; Zhou, J.; Liu, T.; Tao, Y.; Jiang, R.; Liu, M.; Xiao, G.; Zhu, J.; Zhou, Z.-K.; Wang, X.; Jin, C.; Wang, J., Plasmonic gold mushroom arrays with refractive index sensing figures of merit approaching the theoretical limit. *Nature Communications* **2013,** *4*, 2381.

70. Ebbesen, T. W.; Lezec, H. J.; Ghaemi, H. F.; Thio, T.; Wolff, P. A., Extraordinary optical transmission through sub-wavelength hole arrays. *Nature* **1998,** *391*, 667.

71. Li, W.-D.; Hu, J.; Chou, S. Y., Extraordinary light transmission through opaque thin metal film with subwavelength holes blocked by metal disks. *Opt. Express* **2011,** *19* (21), 21098-21108.

72. Zhang, Q.; Hu, P.; Liu, C., Giant-enhancement of extraordinary optical transmission through nanohole arrays blocked by plasmonic gold mushroom caps. *Optics Communications* **2015,** *335* (Supplement C), 231-236.

73. Fan, F.; Chen, M.; Chen, S.; Wang, X. H.; Chang, S. J., Complementary Plasmonic Arrays for Extraordinary Transmission and Modulation of Terahertz Wave. *IEEE Photonics Technology Letters* **2015,** *27* (23), 2485-2488.

74. Lu, B.-R.; Xu, C.; Liao, J.; Liu, J.; Chen, Y., High-resolution plasmonic structural colors from nanohole arrays with bottom metal disks. *Opt. Lett.* **2016,** *41* (7), 1400-1403.

75. Shahin Shahidan, M. F.; Song, J.; James, T. D.; Roberts, A., Multilevel nanoimprint lithography with a binary mould for plasmonic colour printing. *Nanoscale Advances* **2020,** *2* (5), 2177-2184.

76. Murthy, S.; Pranov, H.; Feidenhans, N. A.; Madsen, J. S.; Hansen, P. E.; Pedersen, H. C.; Taboryski, R., Plasmonic color metasurfaces fabricated by a high speed roll-to-roll method. *Nanoscale* **2017,** *9* (37), 14280-14287.

77. Højlund-Nielsen, E.; Clausen, J.; Mäkela, T.; Thamdrup, L. H.; Zalkovskij, M.; Nielsen, T.; Li Pira, N.; Ahopelto, J.; Mortensen, N. A.; Kristensen, A., Plasmonic Colors: Toward Mass Production of Metasurfaces. *Advanced Materials Technologies* **2016,** *1* (7), 1600054.

78. Akinoglu, G. E.; Mir, S. H.; Gatensby, R.; Rydzek, G.; Mokarian-Tabari, P., Block Copolymer Derived Vertically Coupled Plasmonic Arrays for Surface-Enhanced Raman Spectroscopy. *ACS Applied Materials & Interfaces* **2020,** *12* (20), 23410-23416.

79. Clausen, J. S.; Højlund-Nielsen, E.; Christiansen, A. B.; Yazdi, S.; Grajower, M.; Taha, H.; Levy, U.; Kristensen, A.; Mortensen, N. A., Plasmonic Metasurfaces for Coloration of Plastic Consumer Products. *Nano Letters* **2014,** *14* (8), 4499-4504.

80. Ahn, M.-S.; Chung, T.; Jeong, K.-H., Structural coloration of transmission light through self-aligned and complementary plasmonic nanostructures. *Nanoscale* **2018,** *10* (14), 6313-6317.

81. Yue, W.; Gao, S.; Lee, S.-S.; Kim, E.-S.; Choi, D.-Y., Highly reflective subtractive color filters capitalizing on a silicon metasurface integrated with nanostructured aluminum mirrors. *Laser & Photonics Reviews* **2017,** *11* (3), 1600285.

82. Li, S.; Li, W.-D., Refractive index sensing using disk-hole coupling plasmonic structures fabricated on fiber facet. *Opt. Express* **2017,** *25*, 29380.

83. Kotlarek, D.; Fossati, S.; Venugopalan, P.; Gisbert Quilis, N.; Slabý, J.; Homola, J.; Lequeux, M.; Amiard, F.; Lamy de la Chapelle, M.; Jonas, U.; Dostálek, J., Actuated plasmonic nanohole arrays for sensing and optical spectroscopy applications. *Nanoscale* **2020,** *12* (17), 9756-9768.

84. Shen, Y.; Zhou, J.; Liu, T.; Tao, Y.; Jiang, R.; Liu, M.; Xiao, G.; Zhu, J.; Zhou, Z.-K.; Wang, X.; Jin, C.; Wang, J., Plasmonic gold mushroom arrays with refractive index sensing figures of merit approaching the theoretical limit. *Nature Communications* **2013,** *4* (1), 2381.

85. Franklin, D.; Modak, S.; Vázquez-Guardado, A.; Safaei, A.; Chanda, D., Covert infrared image encoding through imprinted plasmonic cavities. *Light: Science & Applications* **2018,** *7* (1), 93.

86. James, T. D.; Mulvaney, P.; Roberts, A., The Plasmonic Pixel: Large Area, Wide Gamut Color Reproduction Using Aluminum Nanostructures. *Nano Letters* **2016,** *16* (6), 3817-3823.

87. Pang, J. S.; Theodorou, I. G.; Centeno, A.; Petrov, P. K.; Alford, N. M.; Ryan, M. P.; Xie, F., Tunable Three-Dimensional Plasmonic Arrays for Large Near-Infrared Fluorescence Enhancement. *ACS Applied Materials & Interfaces* **2019,** *11* (26), 23083-23092.

88. Zang, F.; Su, Z.; Zhou, L.; Konduru, K.; Kaplan, G.; Chou, S. Y., Ultrasensitive Ebola Virus Antigen Sensing via 3D Nanoantenna Arrays. *Advanced Materials* **2019,** *31* (30), 1902331.

89. Peng, Y.; Marcoux, C.; Patoka, P.; Hilgendorff, M.; Giersig, M.; Kempa, K., Plasmonics of thin film quasitriangular nanoparticles. *Applied Physics Letters* **2010,** *96* (13), 133104.

90. Zorić, I.; Zäch, M.; Kasemo, B.; Langhammer, C., Gold, Platinum, and Aluminum Nanodisk Plasmons: Material Independence, Subradiance, and Damping Mechanisms. *ACS Nano* **2011,** *5* (4), 2535-2546.

91. Nordlander, P.; Oubre, C.; Prodan, E.; Li, K.; Stockman, M., Plasmon hybridization in nanoparticle dimers. *Nano letters* **2004,** *4* (5), 899-903.

92. Panchenko, E.; Wesemann, L.; Gómez, D. E.; James, T. D.; Davis, T. J.; Roberts, A., Ultracompact camera pixel with integrated plasmonic color filters. *Advanced Optical Materials* **2019,** *7* (23), 1900893.

93. Zuloaga, J.; Nordlander, P., On the Energy Shift between Near-Field and Far-Field Peak Intensities in Localized Plasmon Systems. *Nano Letters* **2011,** *11* (3), 1280-1283.

94. Ross, B. M.; Lee, L. P., Comparison of near-and far-field measures for plasmon resonance of metallic nanoparticles. *Opt. Lett.* **2009,** *34* (7), 896-898.

95. Langhammer, C.; Yuan, Z.; Zorić, I.; Kasemo, B., Plasmonic Properties of Supported Pt and Pd Nanostructures. *Nano Letters* **2006,** *6* (4), 833-838.

96. Chen, J.; Albella, P.; Pirzadeh, Z.; Alonso-González, P.; Huth, F.; Bonetti, S.; Bonanni, V.; Åkerman, J.; Nogués, J.; Vavassori, P.; Dmitriev, A.; Aizpurua, J.; Hillenbrand, R., Plasmonic Nickel Nanoantennas. *Small* **2011,** *7* (16), 2341-2347.

97. Fan, M.; Lai, F.-J.; Chou, H.-L.; Lu, W.-T.; Hwang, B.-J.; Brolo, A. G., Surface-enhanced Raman scattering (SERS) from Au:Ag bimetallic nanoparticles: the effect of the molecular probe. *Chemical Science* **2013,** *4* (1), 509-515.

98. Liberman, V.; Adato, R.; Jeys, T. H.; Saar, B. G.; Erramilli, S.; Altug, H., Rational design and optimization of plasmonic nanoarrays for surface enhanced infrared spectroscopy. *Optics Express* **2012,** *20* (11), 11953-11967.

99. Otte, M. A.; Estévez, M.-C.; Carrascosa, L. G.; González-Guerrero, A. B.; Lechuga, L. M.; Sepúlveda, B., Improved biosensing capability with novel suspended nanodisks. *The Journal of Physical Chemistry C* **2011,** *115* (13), 5344-5351.

100. Pedram, S.; Kaiyu, W.; Tomas, R.; Anja, B.; Silvan, S., Fabrication and characterization of Au dimer antennas on glass pillars with enhanced plasmonic response. *Nanophotonics* **2017,** *7* (2), 497-505.

101. Major, K. J.; De, C.; Obare, S. O., Recent Advances in the Synthesis of Plasmonic Bimetallic Nanoparticles. *Plasmonics* **2009,** *4* (1), 61-78.

102. Sytwu, K.; Vadai, M.; Dionne, J. A., Bimetallic nanostructures: combining plasmonic and catalytic metals for photocatalysis. *Advances in Physics: X* **2019,** *4* (1), 1619480.

103. Swearer, D. F.; Zhao, H.; Zhou, L.; Zhang, C.; Robatjazi, H.; Martirez, J. M. P.; Krauter, C. M.; Yazdi, S.; McClain, M. J.; Ringe, E.; Carter, E. A.; Nordlander, P.; Halas, N. J., Heterometallic antenna−reactor complexes for photocatalysis. *Proceedings of the National Academy of Sciences* **2016,** *113* (32), 8916-8920.

104. Seemala, B.; Therrien, A. J.; Lou, M.; Li, K.; Finzel, J. P.; Qi, J.; Nordlander, P.; Christopher, P., Plasmon-Mediated Catalytic O2 Dissociation on Ag Nanostructures: Hot Electrons or Near Fields? *ACS Energy Letters* **2019,** *4* (8), 1803-1809.

105. Jackson, J. B.; Halas, N. J., Surface-enhanced Raman scattering on tunable plasmonic nanoparticle substrates. *Proceedings of the National Academy of Sciences of the United States of America* **2004,** *101* (52), 17930-17935.

106. Orendorff, C. J.; Gearheart, L.; Jana, N. R.; Murphy, C. J., Aspect ratio dependence on surface enhanced Raman scattering using silver and gold nanorod substrates. *Physical Chemistry Chemical Physics* **2006,** *8* (1), 165-170.

107. Khoury, C. G.; Vo-Dinh, T., Gold nanostars for surface-enhanced Raman scattering: synthesis, characterization and optimization. *The Journal of Physical Chemistry C* **2008,** *112* (48), 18849-18859.

108. Yu, Q.; Guan, P.; Qin, D.; Golden, G.; Wallace, P. M., Inverted Size-Dependence of Surface-Enhanced Raman Scattering on Gold Nanohole and Nanodisk Arrays. *Nano Letters* **2008,** *8* (7), 1923-1928.

109. Oh, Y.-J.; Kang, M.; Park, M.; Jeong, K.-H., Engineering hot spots on plasmonic nanopillar arrays for SERS: A review. *BioChip Journal* **2016,** *10* (4), 297-309.

110. Wu, K.; Li, T.; Schmidt, M. S.; Rindzevicius, T.; Boisen, A.; Ndoni, S., Gold Nanoparticles Sliding on Recyclable Nanohoodoos—Engineered for Surface-Enhanced Raman Spectroscopy. *Advanced Functional Materials* **2018,** *28* (2), 1704818.

111. Sanger, K.; Durucan, O.; Wu, K.; Thilsted, A. H.; Heiskanen, A.; Rindzevicius, T.; Schmidt, M. S.; Zór, K.; Boisen, A., Large-Scale, Lithography-Free Production of Transparent Nanostructured Surface for Dual-Functional Electrochemical and SERS Sensing. *ACS Sensors* **2017,** *2* (12), 1869-1875.

112. Wu, K.; Rindzevicius, T.; Schmidt, M. S.; Mogensen, K. B.; Xiao, S.; Boisen, A., Plasmon resonances of Ag capped Si nanopillars fabricated using mask-less lithography. *Optics express* **2015,** *23* (10), 12965-12978.

113. Yang, J.; Palla, M.; Bosco, F. G.; Rindzevicius, T.; Alstrøm, T. S.; Schmidt, M. S.; Boisen, A.; Ju, J.; Lin, Q., Surface-Enhanced Raman Spectroscopy Based Quantitative Bioassay on Aptamer-Functionalized Nanopillars Using Large-Area Raman Mapping. *ACS Nano* **2013,** *7* (6), 5350-5359.

114. Kara, S.; Keffous, A.; Giovannozzi, A.; Rossi, A.; Cara, E.; D'Ortenzi, L.; Sparnacci, K.; Boarino, L.; Gabouze, N.; Soukane, S., Fabrication of flexible silicon nanowires by self-assembled metal assisted chemical etching for surface enhanced Raman spectroscopy. *RSC Advances* **2016,** *6* (96), 93649-93659.

115. Men, D.; Wu, Y.; Wang, C.; Xiang, J.; Yang, G.; Wan, C.; Zhang, H., Wafer-Scale Hierarchical Nanopillar Arrays Based on Au Masks and Reactive Ion Etching for Effective 3D SERS Substrate. *Materials (Basel, Switzerland)* **2018,** *11* (2), 239.

116. Gartia, M. R.; Xu, Z.; Behymer, E.; Nguyen, H.; Britten, J. A.; Larson, C.; Miles, R.; Bora, M.; Chang, A. S.; Bond, T. C., Rigorous surface enhanced Raman spectral characterization of large-area high-uniformity silver-coated tapered silica nanopillar arrays. *Nanotechnology* **2010,** *21* (39), 395701.

117. Caldwell, J. D.; Glembocki, O. J.; Bezares, F. J.; Kariniemi, M. I.; Niinistö, J. T.; Hatanpää, T. T.; Rendell, R. W.; Ukaegbu, M.; Ritala, M. K.; Prokes, S. M.; Hosten, C. M.; Leskelä, M. A.; Kasica, R., Large-area plasmonic hot-spot arrays: sub-2 nm interparticle separations with plasma-enhanced atomic layer deposition of Ag on periodic arrays of Si nanopillars. *Optics Express* **2011,** *19* (27), 26056-26064.

118. Hu, M.; Ou, F. S.; Wu, W.; Naumov, I.; Li, X.; Bratkovsky, A. M.; Williams, R. S.; Li, Z., Gold nanofingers for molecule trapping and detection. *Journal of the American Chemical Society* **2010,** *132* (37), 12820-12822.

119. Li, T.; Wu, K.; Rindzevicius, T.; Wang, Z.; Schulte, L.; Schmidt, M. S.; Boisen, A.; Ndoni, S., Wafer-Scale Nanopillars Derived from Block Copolymer Lithography for Surface-Enhanced Raman Spectroscopy. *ACS Applied Materials & Interfaces* **2016,** *8* (24), 15668-15675.

120. De Angelis, F.; Gentile, F.; Mecarini, F.; Das, G.; Moretti, M.; Candeloro, P.; Coluccio, M. L.; Cojoc, G.; Accardo, A.; Liberale, C.; Zaccaria, R. P.; Perozziello, G.; Tirinato, L.; Toma, A.; Cuda, G.; Cingolani, R.; Di Fabrizio, E., Breaking the diffusion limit with super-hydrophobic delivery of molecules to plasmonic nanofocusing SERS structures. *Nature Photonics* **2011,** *5*, 682.

121. Kamińska, A.; Witkowska, E.; Winkler, K.; Dzięcielewski, I.; Weyher, J. L.; Waluk, J., Detection of Hepatitis B virus antigen from human blood: SERS immunoassay in a microfluidic system. *Biosensors and Bioelectronics* **2015,** *66*, 461-467.

122. Li, J.; Chen, C.; Jans, H.; Xu, X.; Verellen, N.; Vos, I.; Okumura, Y.; Moshchalkov, V. V.; Lagae, L.; Van Dorpe, P., 300 mm Wafer-level, ultra-dense arrays of Au-capped nanopillars with sub-10 nm gaps as reliable SERS substrates. *Nanoscale* **2014,** *6* (21), 12391-12396.

123. Ghoshal, T.; Senthamaraikannan, R.; Shaw, M. T.; Holmes, J. D.; Morris, M. A. J. N., "In situ" hard mask materials: a new methodology for creation of vertical silicon nanopillar and nanowire arrays. *Nanoscale* **2012,** *4* (24), 7743-7750.

124. Mokarian-Tabari, P.; Vallejo-Giraldo, C.; Fernandez-Yague, M.; Cummins, C.; Morris, M. A.; Biggs, M. J. P., Nanoscale neuroelectrode modification via sub-20 nm silicon nanowires through self-assembly of block copolymers. *Journal of Materials Science: Materials in Medicine* **2015,** *26* (2), 120.

125. Eustis, S.; El-Sayed, M. A., Determination of the aspect ratio statistical distribution of gold nanorods in solution from a theoretical fit of the observed inhomogeneously broadened longitudinal plasmon resonance absorption spectrum. *Journal of Applied Physics* **2006,** *100* (4), 044324.

126. Kim, K.; Yoon, J. K., Raman Scattering of 4-Aminobenzenethiol Sandwiched between Ag/Au Nanoparticle and Macroscopically Smooth Au Substrate. *The Journal of Physical Chemistry B* **2005,** *109* (44), 20731-20736.

127. Huang, Y.-F.; Zhu, H.-P.; Liu, G.-K.; Wu, D.-Y.; Ren, B.; Tian, Z.-Q., When the signal is not from the original molecule to be detected: chemical transformation of para-aminothiophenol on Ag during the SERS measurement. *Journal of the American Chemical Society* **2010,** *132* (27), 9244-9246.

128. Mahajan, S.; Cole, R. M.; Speed, J. D.; Pelfrey, S. H.; Russell, A. E.; Bartlett, P. N.; Barnett, S. M.; Baumberg, J. J., Understanding the Surface-Enhanced Raman Spectroscopy "Background". *The Journal of Physical Chemistry C* **2010,** *114* (16), 7242-7250.

129. Ding, S.-Y.; You, E.-M.; Tian, Z.-Q.; Moskovits, M., Electromagnetic theories of surface-enhanced Raman spectroscopy. *Chemical Society Reviews* **2017,** *46* (13), 4042-4076.

130. Fu, Q.; Zhan, Z.; Dou, J.; Zheng, X.; Xu, R.; Wu, M.; Lei, Y., Highly Reproducible and Sensitive SERS Substrates with Ag Inter-Nanoparticle Gaps of 5 nm Fabricated by Ultrathin Aluminum Mask Technique. *ACS Applied Materials & Interfaces* **2015,** *7* (24), 13322-13328.

131. Ataka, K.; Heberle, J., Functional vibrational spectroscopy of a cytochrome c monolayer: SEIDAS probes the interaction with different surface-modified electrodes. *Journal of the American Chemical Society* **2004,** *126* (30), 9445-9457.

132. Le Ru, E.; Blackie, E.; Meyer, M.; Etchegoin, P. G., Surface enhanced Raman scattering enhancement factors: a comprehensive study. *The Journal of Physical Chemistry C* **2007,** *111* (37), 13794-13803.

133. Tahir, M. A.; Zhang, X.; Cheng, H.; Xu, D.; Feng, Y.; Sui, G.; Fu, H.; Valev, V.; Zhang, L.; Chen, J.-M., Klarite as Label-Free SERS-Based Assay: A Promising Approach for Atmospheric Bioaerosol Detection. *The Analyst* **2019,** *145*.

134. Oo, S.; Chen, R.; Siitonen, S.; Kontturi, V.; Eustace, D.; Tuominen, J.; Aikio, S.; Charlton, M., Disposable plasmonic plastic SERS sensor. *Optics express* **2013,** *21* (15), 18484-18491.

135. Ferrarese Lupi, F.; Giammaria, T.; Volpe, F.; Lotto, F.; Seguini, G.; Pivac, B.; Laus, M.; Perego, M., High aspect ratio PS-b-PMMA block copolymer masks for lithographic applications. *ACS applied materials & interfaces* **2014,** *6* (23), 21389-21396.

136. Hölke, A.; Henderson, H. T., Ultra-deep anisotropic etching of (110) silicon. *Journal of Micromechanics and Microengineering* **1999,** *9* (1), 51-57.

137. Miyake, H.; Ye, S.; Osawa, M., Electroless deposition of gold thin films on silicon for surface-enhanced infrared spectroelectrochemistry. *Electrochemistry Communications* **2002,** *4* (12), 973-977.

138. Durucan, O.; Rindzevicius, T.; Schmidt, M. S.; Matteucci, M.; Boisen, A., Nanopillar filters for surface-enhanced Raman spectroscopy. *ACS sensors* **2017,** *2* (10), 1400-1404.

139. Khan, M. S.; Dosoky, N. S.; Williams, J. D., Engineering Lipid Bilayer Membranes for Protein Studies. *International Journal of Molecular Sciences* **2013,** *14* (11), 21561-21597.

140. Adato, R.; Altug, H., In-situ ultra-sensitive infrared absorption spectroscopy of biomolecule interactions in real time with plasmonic nanoantennas. *Nature Communications* **2013,** *4*, 2154.

141. Gole, A.; Sainkar, S. R.; Sastry, M., Electrostatically Controlled Organization of Carboxylic Acid Derivatized Colloidal Silver Particles on Amine-Terminated Self-Assembled Monolayers. *Chemistry of Materials* **2000,** *12* (5), 1234-1239.